Sustainable Engineering Novit
https://www.sciltp.com/journals/sen

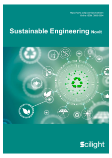

Review

Unlocking the Potential of MOFs for Waste Plastic Resource Utilization and Microplastic Pollution Control

Yichun Su [1,†], Yuxin Shi [2,†], Liujun Jin [1,3], Yuan Lu [1], Jinpeng Wang [4], Hyeonseok Yoon [5,*] and Ping Liu [1,3,*]

[1] School of Petrochemical Engineering, Changzhou University, Changzhou 213164, China
[2] School of Materials Science and Engineering, Suzhou University of Technology, Changshu 215500, China
[3] Jiangsu Province Engineering Research Center of Biodegradable Materials, Changzhou University, Changzhou 213164, China
[4] School of Materials Science and Engineering, Changzhou University, Changzhou 213164, China
[5] School of Polymer Science and Engineering, Chonnam National University, Gwangju 61186, Republic of Korea
* Correspondence: hyoon@chonnam.ac.kr (H.Y.); pingliu@cczu.edu.cn (P.L.)
† These authors contributed equally to this work.

How To Cite: Su, Y.; Shi, Y.; Jin, L.; et al. Unlocking the Potential of MOFs for Waste Plastic Resource Utilization and Microplastic Pollution Control. *Sustainable Engineering Novit* **2026**, *2*(1), 4. https://doi.org/10.53941/sen.2026.100004

Received: 24 November 2025
Revised: 6 January 2026
Accepted: 27 January 2026
Published: 6 March 2026

Abstract: The global plastic waste crisis urgently calls for innovative strategies that move beyond conventional disposal methods. Against this backdrop, establishing a circular pathway for plastic waste—effectively converting end-of-life products into valuable resources—has become a critical objective for sustainable development. Metal–organic frameworks (MOFs) have emerged as a revolutionary catalytic platform, offering unique advantages such as structural tunability, ultrahigh surface area, and precisely designable active sites, thereby opening new possibilities for achieving this goal. This review highlights the great potential of MOF-based catalysts in addressing key challenges during plastic valorization and explores their role as ideal drivers for such a circular plastic pathway. It systematically summarizes synthesis strategies for MOFs and recent advances in their catalytic applications, covering pathways for converting plastics into high-value monomers or chemicals, as well as efficient microplastic degradation. The core objective is to demonstrate how MOF-enabled catalysis can bridge waste plastics and renewable resources, thereby providing strategic support for building a circular plastic economy.

Keywords: MOFs; circular economy; plastics; chemical recycling; adsorption

1. Introduction

Plastics have seen widespread use since their inception, with their fossil fuel origins tracing back to the Industrial Revolution [1–4]. Plastics are high molecular polymers fabricated from small molecule monomers and are well-known for their chemical stability, durability, and ease of processing [5,6]. However, the long lifespan of plastics has also led to a global environmental crisis, as they are solid polymers connected by covalent bonds and cannot usually be depolymerized by biological or non-biological means in landfills or natural environments [7]. Plastics Europe estimates 413.8 million tons of plastic were produced globally in 2023, with the stark reality that under 10% is recycled, leaving a staggering 79% to be landfilled or released into the environment [8]. By 2050, global plastic production will exceed 34 billion tons [9]. Developing effective plastic recycling strategies and reintegrating waste plastic into industrial systems is crucial for the sustainable use of plastic [10].

Plastics recycling can be categorized into three levels: physical recycling, chemical recycling, and energy recovery (incineration) [11,12]. To date, the main commercial plastic products worldwide are polyethylene (PE), polystyrene (PS), polypropylene (PP), polyethylene terephthalate (PET), polyvinyl chloride (PVC), and so on (Figure 1) [13]. These plastics differ significantly in their chemical structure and physical properties. Physical recycling exhibits limitations in terms of the number of recycling cycles, as most recycling and reprocessing systems require single-component plastics to ensure the quality of recycled products [14]. However, mechanical recycling is susceptible to impurities and polymer chain degradation in downstream products due to its thermal-mechanical processing [15]. While incineration can recover some plastics, it also produces large amounts of CO_2, which is contrary to environmental protection efforts [16–18]. Chemical recycling converts plastic waste into monomers or small molecules for the production of new plastics or other industrial feedstocks [19]. For complex multi-material plastics, chemical recycling is promising in breaking the boundaries of plastic production and can handle low-value waste plastics [20–22].

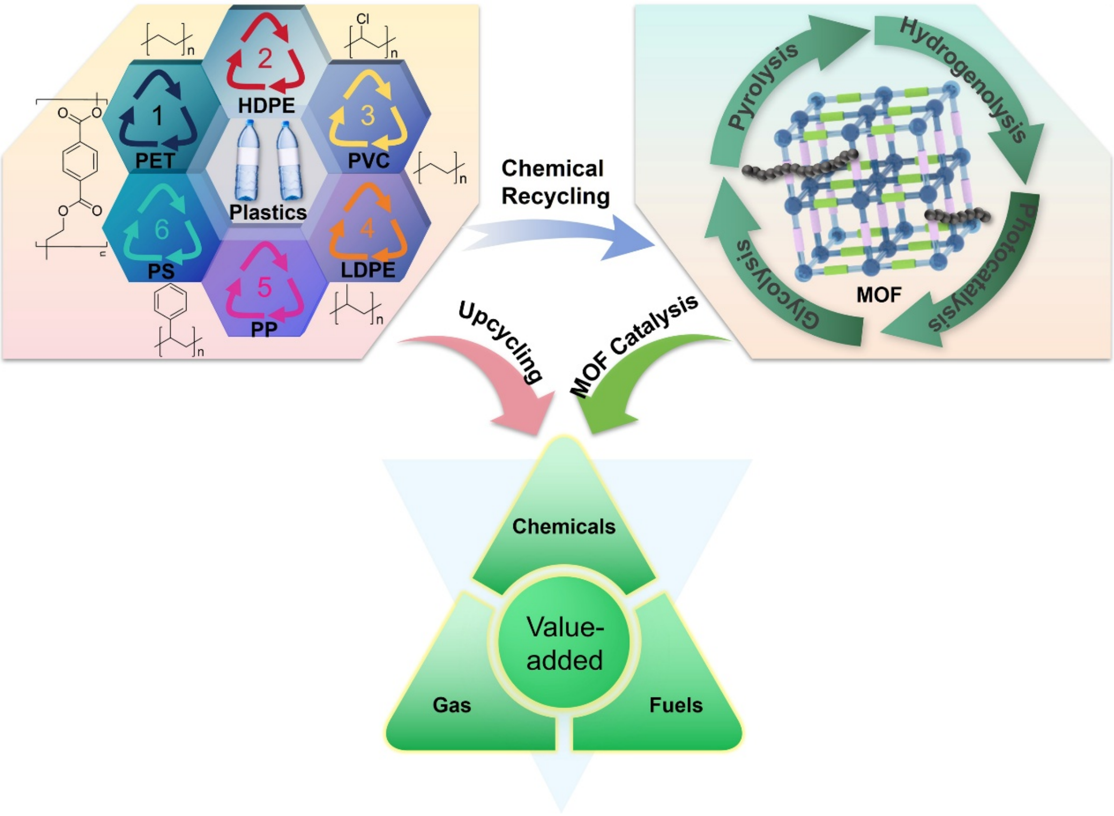

Figure 1. Schematic diagram of chemical recycling of plastic waste catalyzed by MOF.

In chemical recycling processes like catalytic cracking, and hydrogenolysis, catalysts are key to enhancing reaction efficiency and product selectivity [23,24]. Zeolites, metal oxides, or loaded noble metal catalysts offer high stability and easy separation [25–27]. Among these, zeolites exhibit outstanding thermal stability and Brønsted acidity, enabling effective plastic cracking [28]. As a result, zeolites are the traditional choice in high temperature pyrolysis and glycolysis reactions [29]. In spite of the challenges, achieving high product selectivity, narrow distribution control, and expanding product diversity using limited raw materials have become key objectives [30]. It requires new catalysts to possess specific capabilities while maintaining sufficient thermal stability for easy recovery and reuse. In turn, it drives the demand for highly designable catalysts whose structures can be precisely customized for different reactions [31–33].

This trend is driving the emergence of metal-organic frameworks (MOFs) as porous materials that differ significantly from zeolite structures [34]. The unique structural designability of MOF renders them a promising new catalytic platform for polymer degradation [35,36]. As a typical representative of reticular chemistry, the key to MOF design is based on the concept that "a network is composed of vertices and edges" [37–39]. By systematically adjusting the porosity of MOF (specific surface area, specific pore volume, porosity, and pore size) through secondary building units (SBUs) and charged ligands, their catalytic performance can be influenced [40–42]. In contrast, altering the pore size of zeolites is relatively challenging, and the chemical properties of their tetrahedral structural units to some extent limit their development [43]. Over the past few decades, the enormous structural diversity and modular tailoring capabilities of MOF have led to rapid development in research [44,45]. However, most reported MOFs are predominantly microporous, thus constraining their utility in processing bulky molecules.

Herein, we showcase the latest design strategies for microporous/mesoporous MOF and their application in plastic catalysis. We also discuss in detail how MOF can be used in degradation reactions (alcoholysis, hydrolysis, pyrolysis, and photocatalysis) of various types of plastics and in the adsorption of microplastics. Last but not least, we will focus on the key breakthrough areas in the future development of MOF catalysts.

2. Design Rationale and Synthesis Strategy

The origin of MOFs in the mid-1990s marked a milestone in porous materials science [46]. The highly ordered, crystalline 3D network structure endows MOFs with a large number of regularly arranged cavities and channels [47,48]. This property provides a new type of material with great potential for various applications based on its unique pore characteristics [49].

The synthesis of MOFs typically comprises the following critical stages: coordination bonding, crystal nucleation, and crystal growth [50]. In suitable reaction systems, metal ions or SBUs first coordinate with organic ligands, constructing the primary structural frameworks [51]. This step directly determines the basic connectivity and geometric shape of MOFs. The initial nucleation event is triggered by coordination bond formation, which subsequently yields stable microcrystalline nuclei [52]. The nucleation kinetics of this stage (controlled by concentration, temperature and solvent) are critical for the size distribution and density of crystal nuclei, thereby pre-determining the final microstructure of MOFs [53]. Following nucleation, crystal growth occurs as the subsequent stage, with its rate having a key influence on the grain size and defect density of the product [54,55]. The macro-scale characteristics of the material, including its porosity and structural stability, are dictated by the entirety of this journey [56,57].

The domain of MOF remains a highly dynamic area of research [58–60]. Scholars are endeavoring to advance future scientific and industrial pursuits through the design of novel frameworks, the resolution of paramount stability issues, and the creation of innovative synthetic routes [61,62].

2.1. Direct Synthesis Method

The direct synthesis approach represents a foundational and versatile strategy for constructing MOFs in a single step [63,64]. Unlike post-synthetic modifications, which often involve complex treatments that can compromise crystallinity, direct methods aim to program the porosity directly into the crystalline framework during its self-assembly [65–67]. This is primarily achieved by ingeniously introducing structural-directing agents or by employing sophisticated ligand design to create inherent imbalances and defects [68,69]. The paramount advantage of these bottom-up techniques is the precise control over the hierarchy, often yielding well-defined, interconnected pore systems with maintained crystallinity and enhanced stability [70]. The following sections will delve into four principal pillars of this approach: the use of templating agents, the rational design of organic linkers, defect engineering, and strategies for inducing assembly, discussing their mechanisms, design principles, and the remarkable structural diversity they enable.

2.1.1. Template Method

The templating approach represents one of the most potent and direct methodologies for engineering ordered mesoporous and macroporous architectures into MOFs [71,72]. The core concept relies on utilizing a sacrificial agent—a “template” possessing a predefined pore structure—to guide the confined nucleation and oriented growth of MOFs [73]. Subsequent removal of the template via physical or chemical methods results in the replication of its porous network within the MOF matrix [74].

Depending on their intrinsic properties, templates are mainly divided into two distinct categories: soft templates and hard templates. In particular, the hard template method is the most powerful tool for constructing long-range ordered multi-level porous MOFs [75]. Its core principle involves using a pre-synthesized rigid material with a specific nanostructure as a sacrificial template to guide the targeted MOF to grow and crystallize in a directed manner on its surface or within its pores [76]. The template is then selectively removed via chemical or physical methods, resulting in MOF materials that replicate the template’s morphology or possess special pore structures [77]. Typical hard template materials include SiO_2, polymer microspheres, hydroxides, and other MOFs [78–83].

The topological properties of porous materials—particularly the pore size in each dimension and their size uniformity—are critical determinants of their performance in specific applications [84]. The development of highly ordered mesoporous and macroporous crystalline frameworks remains a major research objective, particularly with respect to achieving larger pore sizes in MOFs [85,86]. Employing a combined strategy of polystyrene nanosphere templating and dual-solvent-induced nucleation, Li’s team enabled the creation of MOF structures with highly oriented and ordered macropores [78]. This synthesis strategy can be broadly divided into four steps (Figure 2a). First, monodisperse PS microspheres are assembled into highly ordered 3D bulk structures; then the interstices are filled with ZIF-8 precursors; next, the bulk material is immersed in a methanol/ammonia water dual solvent for controlled crystallization of the MOF; finally, the template is removed to obtain ordered macro-microporous MOF single-crystal materials, which the researchers named SOM-ZIF-8 (SOM stands for single-crystal ordered macropore). The scanning electron microscopy (SEM) characterization revealed that SOM-ZIF-8 adopts a regular tetrahedral structure, with macropores exhibiting clear 3D ordered oriented arrangements (Figure 2b,c). This work pioneered the development of 3D ordered macro–microporous materials, systems simultaneously featuring macropores and micropores. The synergistic process allows MOFs to grow within the ordered voids, forming single crystals with a well-aligned macro–microporous architecture. These hierarchical frameworks demonstrate significantly superior catalytic activity and recyclability in macromolecular reactions compared to traditional polycrystalline or disordered macroporous ZIF-8.

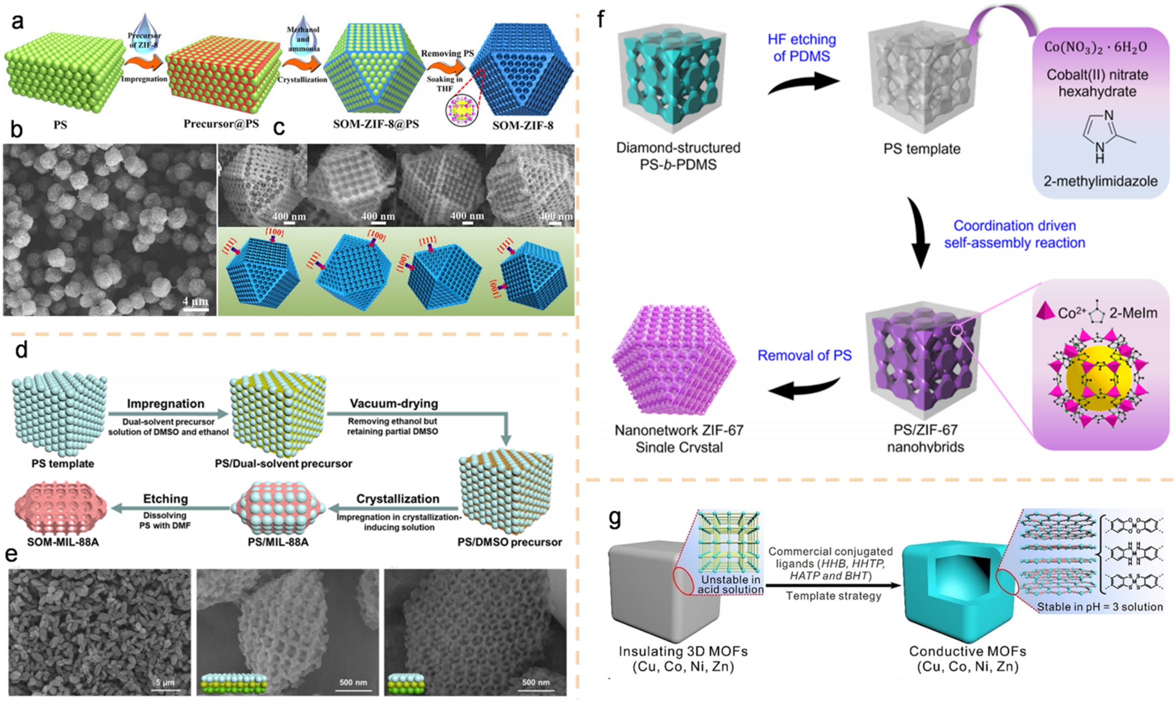

Figure 2. (**a**–**c**) Schematic diagram of ZIF-8 design and representative SEM images [78]. Copyright 2018, AAAS. (**d**,**e**) SOM-MIL-88A synthesis scheme diagram and representative SEM images [82]. Copyright 2024, American Chemical Society. (**f**) Schematic diagram of the preparation of ZIF-67 single crystal by template coordination-driven self-assembly reaction [83]. Copyright 2025, American Chemical Society. (**g**) Schematic diagram of the transformation from insulating 3D MOF to 2D c-MOF [87]. Copyright 2024, Wiley.

Based on the PS template, Du's research group used non-protonic solvents to stabilize the precursor solution and control the crystallization process, successfully synthesizing SOM-MIL-88A with stability in water and acid solutions [82]. By adjusting the DMSO content, the crystal attachment and Ostwald ripening processes can be balanced to obtain the desired SOM-MIL-88A morphology (Figure 2d). This solves the two major challenges of precursor stabilization and crystallization modulation. The SEM image shows that SOM-MIL-88A has a spindle-shaped morphology, and the individual crystals in different directions reveal a clear 3D ordered macroporous structure (Figure 2e). Ho et al. fabricated periodic 3D nanostructured materials by infiltrating suitable precursors into nanoporous templates, curing them into a rigid framework, and then removing the templates [83]. Using a PS template etched from polystyrene-*b*-polydimethylsiloxane (PS-*b*-PDMS), mesoporous ZIF-67 with a nano-network structure was obtained (Figure 2f). This structure enhances the accessibility of active sites in mesoporous MOFs, enabling the transition from brittle to ductile MOFs, thereby offering promising catalytic applications. Additionally, Dong and colleagues utilized insulating 3D MOFs as precursors and employed conjugated ligand-induced conversion to synthesize 2D conjugated metal-organic frameworks (2D C-MOFs) with hierarchical porous nanostructures [87]. This process occurs spontaneously at room temperature, involving a two-step reaction between the precursor, an amorphous intermediate, and the product, enabling precise replication of the precursor morphology while enhancing crystallinity and porosity (Figure 2g).

In contrast, the soft template method utilizes amphiphilic molecules (such as surfactants, block copolymers, or emulsions) that spontaneously organize into specific ordered structures in solution as "templates" to guide the crystallization of MOF precursors at their interfaces or surroundings, thereby creating mesoporous or macroporous structures. The soft template method shows great potential in terms of simplifying synthesis and flexibility, but its successful application strongly depends on the development of new template molecules that can remain stable in the MOF synthesis environment. Zhao's team successfully constructed a three-dimensional (3D) core-satellite-like superstructure on the SiO_2 interface using extremely small polymeric micelles (approximately 18 nm) as basic "Lego-like" building blocks, by precisely controlling electrostatic interactions [88]. The researchers utilized a triblock copolymer polymeric polystyrene-*block*-poly(4-vinylpyridine)-*block*-poly(ethylene oxide) (PS-PVP-PEO) to form uniform, stable micelles in water as the basic building blocks (Figure 3a). These micelles exhibit a core-shell structure, with the PVP and PEO segments in the shell layer providing abundant interaction sites. To assemble the superstructure, the negatively charged single micelles were introduced to a dispersion of positively charged colloidal SiO_2 spheres. The surface charge density of the SiO_2 spheres was precisely controlled by varying the concentration of ammonia water. This regulation enabled fine-tuning of the electrostatic attractive forces between the micelles and the SiO_2 substrates, while simultaneously modulating the repulsive forces between adjacent micelles. The number of micelles in this structure can be quantitatively controlled, providing new insights for designing multi-scale, multi-level functional materials and devices. Building upon their previous research on micelles, Zhao's team recently integrated a hard-templating approach to synthesize a class of single-crystalline mesoporous MOFs (meso-MOFs) with hollow and multilevel pore structure [89]. By adjusting HCl/CH_3COOH ratio, the pH of the reaction system was precisely controlled, allowing regulation of the dissolution kinetics of acid-sensitive seeds that served as hard templates for the hollow structures (Figure 3b). Simultaneously, the concentrations of the two acids modulated the growth kinetics of the mesoporous MOF shell. This dual control strategy successfully balanced the crystallization integrity and the precise manipulation of the hierarchical architecture.

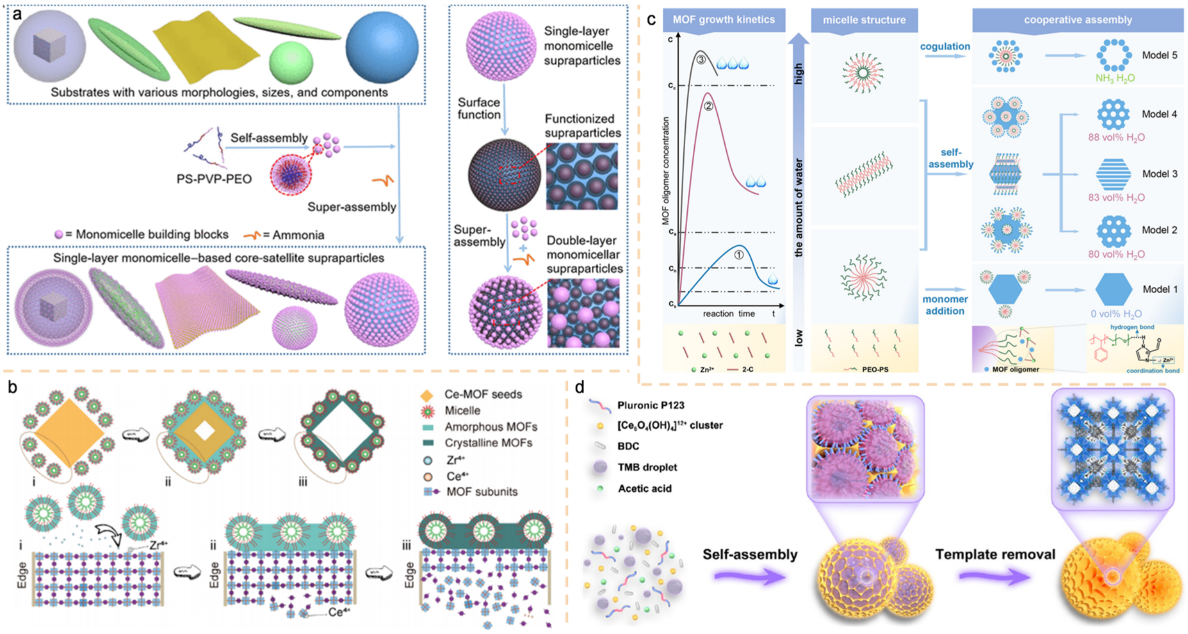

Figure 3. (**a**) The single micellar interface super-assembly pathway enables the modularization of single micelles [88]. Copyright 2022, AAAS. (**b**) The single micellar interface super-assembly pathway enables the modularization of single micelles [89]. Copyright 2025, American Chemical Society. (**c**) Schematic diagram illustrating the influence of water volume on the micelle assembly and micelle structure mediated by MOF kinetics [90]. Copyright 2025, Wiley. (**d**) Schematic diagram of the formation of layered porous nanoparticles [91]. Copyright 2023, American Chemical Society.

Currently, the soft template method based on micelle assembly is widely recognized for its highly tunable mesoscopic structure. The Chao and Luo team proposed a dynamics-mediated micelle assembly strategy, achieving the universal preparation of various zeolite imidazolate framework (ZIF) single-crystal mesoporous materials such as ZIF-90, ZIF-8, and ZIF-67 [90]. The strategic use of water accelerates MOF kinetic-mediated micelle assembly by promoting ligand deprotonation, thereby inhibiting MOF self-growth and achieving synergistic assembly between micelles and MOFs. Furthermore, by regulating the Flory-Huggins interaction parameters between the solvent and micelles through water content control, multi-level pore structures ranging from spherical, cylindrical to vesicular shapes can be precisely constructed (Figure 3c). Guan et al. reached the controlled synthesis of various novel UiO-66 nanostructures with rich geometric shapes and asymmetric hierarchical porous structures by adjusting the concentration of the amphiphilic triblock copolymer template

Pluronic P123 (Figure 3d) [91]. The enhanced catalytic activity of these nanoparticles in CO_2 cycloaddition, compared to microporous UiO-66 nanocrystals, is attributed to their tunable structural symmetry and integrated macro-meso-microporous networks.

2.1.2. Ligand Design Method

Ligands serve as the molecular blueprint for MOFs, and their design is central to research, precisely defining the material's microstructure, pore characteristics, stability mechanisms, and functional applications. The core strategy for constructing the target topological network is to select ligands with specific symmetry and coordination point numbers (functional groups). The geometric shape of the ligand "guides" the formation of specific SBUs by metal clusters, which ultimately assemble into the target topological structure with specific pore sizes and pore shapes (such as cage-like or tubular).

Ultra-microporous materials (pore size < 7 Å) exhibit highly sensitive molecular-size-selective screening properties, making them crucial in catalysis, gas separation, batteries, and so on. Unfortunately, traditional ultra-microporous materials like carbon materials, oxides, and zeolites inherently lack uniform pore size and structural tunability. In contrast, Zr-MOFs, which combine high stability and scalability, have emerged as a research hotspot in recent years. The Wang team proposed a structural control strategy based on high coordination density multidentate carboxylate ligands and successfully constructed 10 new types of ultra-microporous Zr-MOFs [92]. By controlling the geometric configuration and connectivity of the ligands, the authors achieved precise control of pore size (4.5–6.8 Å). The length of the ligands (defined as the distance between the two farthest carboxylate carbons) shows weak correlation with MOF pore size, and simply elongating the ligands does not yield smaller pore sizes. Figure 4a shows the crystal structures and topologies of four octadentate ligand-based Zr-MOFs (HIAM-801–804). HIAM-801–804 are all low-connectivity (4-c or 8-c) Zr_6 nodes with a **scu** topology. Despite their low node connectivity, these structures form stable ultramicroporous frameworks due to the high ligand coordination density. The representative material HIAM-802 can achieve precise separation of C_6 alkane isomers. This work goes beyond expanding MOF structural diversity to offer a universal design strategy for the future development of separation technologies.

Later, based on the concept of high-connectivity ligands, the team successfully synthesized a series of porous alkali metal organic frameworks (AMOFs) encompassing Li, Na, K, Rb, and Cs (Hiam-112-Li/Na/K/Rb/Cs) using octacarboxylic acid ligands (H_8TDBPB) as the key component [93]. By inhibiting the coordination of alkali metals with solvents and promoting their connection with organic ligands, a stable 3D porous structure was formed. HIAM-112-Li/Na/K/Rb/Cs all belong to the monoclinic crystal system and have similar space groups, but their coordination patterns, structural units, and connectivity exhibit significant differences (Figure 4b). Notably, HIAM-112-Na/K/Rb exhibits a stable framework structure and high porosity, along with excellent adsorption-desorption stability. The current work validates the effectiveness of the proposed strategy in constructing AMOFs with permanent porosity and high stability.

The construction of highly connected MOFs poses a major synthetic challenge in reticular chemistry. Focusing on the study of highly connected organic ligands, Chen's research group designed a dodecacarboxylic acid ligand (H_{12}HDTB) with carboxyl groups precisely distributed at the 12 vertices of a hexagonal prism, encoding the geometric information of the target network [94]. In topology, assembling 12-connected nodes with 4-connected and 6-connected nodes yields (4,12)-connected square and hexagonal prism (**shp)** and (6,12)-connected trigonal prism and hexagonal prism (**alb)** networks. In this configuration, the 12 carboxyl groups of the ligand H_{12}HDTB are positioned at the 12 vertices of a hexagonal prism, with the entire ligand adopting a hexagonal prism geometric structure (Figure 4c). Additionally, when the ligand H_{12}HDTB is assembled with metal clusters of different geometric configurations, a series of **shp** and **alb**-derived topological networks are obtained. As early as 2024, they utilized the hetero-supermolecular-building-block (Hetero-SBBs) strategy to simultaneously introduce two types of metal-organic polyhedra as building blocks in the network structure, synthesizing a new MOF (**uru**-MOF) with three distinct node types [95]. Topologically, the **uru** network structure is generated by replacing the 8-connected nodes in the **bcu**-b network with the 12-connected node and 3-connected node (Figure 4d). Therefore, the uru network can be deconstructed into 3-connected nodes, 12-connected nodes, and 24-connected nodes, which correspond to triangular, cuboctahedral, and rhombohedral polyhedra, respectively. The authors propose a concept of Hetero-SBBs that transcends traditional approaches, and apply it to the preparation of high-connectivity MOFs based on multi-metal organic cages. This not only expands the theoretical framework of grid chemistry and supramolecular building block strategies but also provides a pioneering platform for the controlled synthesis of next-generation high-porosity metal-organic frameworks.

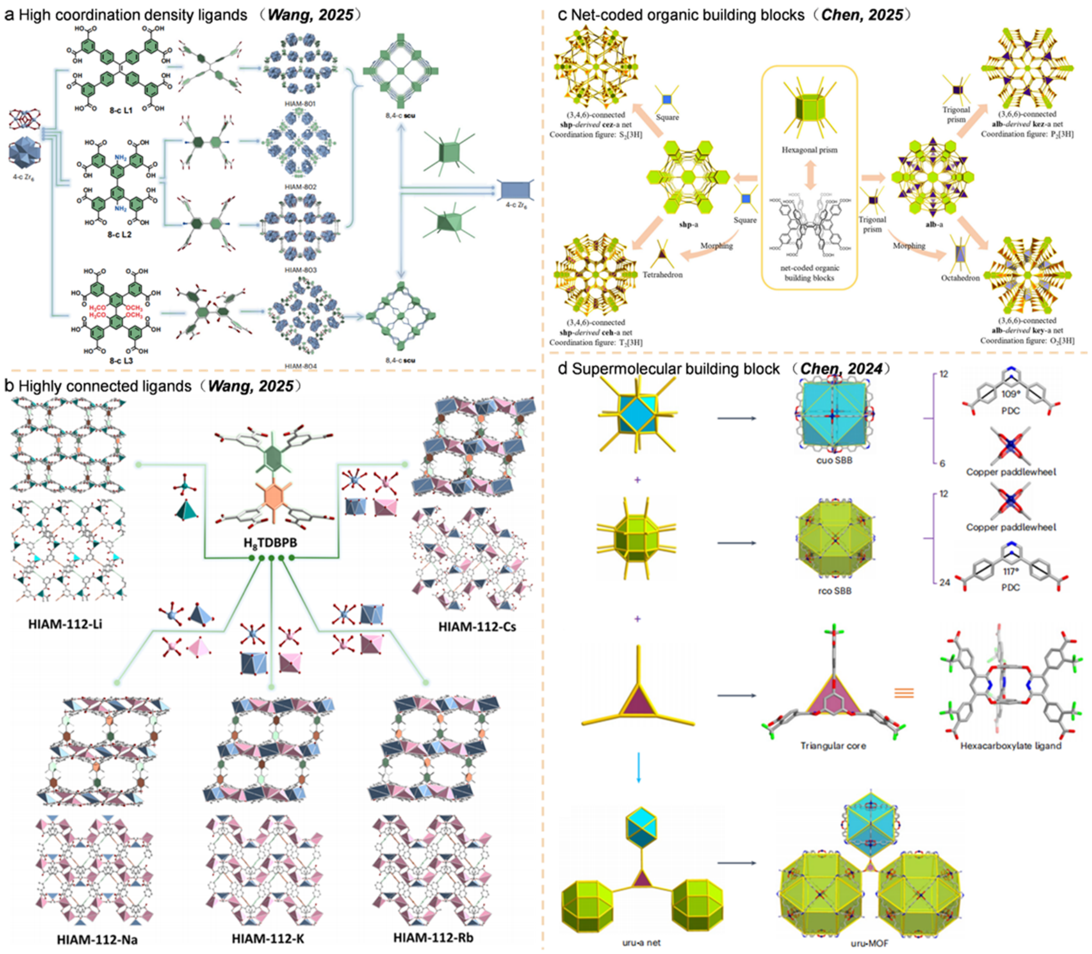

Figure 4. (**a**) Crystallographic structure of HIAM-801 through HIAM-804 built on octacarboxylates [92]. Copyright 2025, Nature. (**b**) Crystal structures of HIAM-112-Li/Na/K/Rb/Cs [93]. Copyright 2025, American Chemical Society. (**c**) Net-coded organic building blocks for the assembly of **shp-**, **alb-**, and their derived networks [94]. Copyright 2025, American Chemical Society. (**d**) A hetero-SBB strategy for the synthesis of uru-MOF [95]. Copyright 2024, Nature.

2.1.3. Defective Engineering

Traditionally, crystal defects have been regarded as detrimental factors that compromise material performance. However, for MOFs, research has revealed that moderate, ordered defects can create novel functionalities unattainable in perfect crystals—akin to a "transmutation of base metal into gold". Through intentional and controlled introduction of structural defects into MOF crystal lattices, their physicochemical properties—such as pore environment, electronic structure, stability, and catalytic active sites—can be precisely engineered. Defect engineering has transformed MOFs from materials pursuing "perfection" into customizable "functional platforms".

Defects in MOFs primarily occur in the ligands. The absence of linkers generates larger mesopores (2–50 nm), overcoming the inherent limitation of MOFs being dominated by micropores (<2 nm). This facilitates the transport and diffusion of macromolecules. Yet constructing MOF materials with precisely tailored pore sizes for specific applications remains challenging. In 2017, the Zhou team reported a method termed "linker labilization" which builds upon linker installation and solvent-assisted ligand doping [96,97]. Linker labilization represents the reverse of linker installation. In this process, MOF is first synthesized using the pro-labile linker and coordinatively saturated clusters. Under acidic conditions, these pro-labile organic linkers undergo cleavage, breaking apart into two monocarboxylate fragments that can be removed, thereby generating defects within the framework (Figure 5a). Researchers constructed MOF materials containing varying proportions of pre-deactivated linking groups. By rationally controlling the content of pre-stabilized linkers and acid concentration, the maximum pore size was adjusted from 1.5 nm to 18 nm. It is demonstrated that this method can generate layered porous MOFs under stable conditions. Similarly drawing on linker labilization principles, Huang's team employed the pre-unstable linker 4,4'-oxalyldibenzoate (ODB), which fractures under acidic conditions to decompose into two removable monocarboxylic acid molecules [98]. This precisely creates defect sites within the framework, representing a more sophisticated defect-building approach compared to traditional decarboxylation or chemical etching (Figure 5b). To conclusively validate these engineered defect structures, the researchers employed aberration-corrected scanning transmission electron microscopy combined with low-dose high-angle annular dark-field STEM imaging technique. By visualizing defects such as vacancies and distortions caused by missing linkers or metal nodes within the crystal structure, they clearly distinguished between pristine crystals and defect-bearing structures. The use of defect-rich d-Zr-ODB-hz as a support for Pd furnished the fully hydrogenated alkanes with complete selectivity. Merely altering the defect structure within the MOF carrier enabled switching of the catalytic reaction pathway. The introduction of defects fundamentally altered the catalyst's electronic properties and reaction microenvironment, ultimately enabling precise "switching" control over catalytic selectivity.

Beyond linker defects, ligand vacancies at metallic nodes can generate unsaturated metal sites. Yang's team introduced metal vacancies into the 12-connected {Ti_8} rings via a titanium-deficient source, accompanied by uncoordinated carboxylate oxygen, resulting in the formation of MIL-125 defects [99,100]. These sites function as inherent "structural defects". MIL-125-X (X = Mn, Fe, Co, Ni, Cu, Zn), were synthesized by decorating the metal vacancies in MIL-125-defect with single-atom metal centers such as Zn(II) (along with Mn, Fe, Co, Ni, Cu) (Figure 5c). The focus of this work is on the most promising MIL-125-Zn. The introduction of defects does not merely create additional adsorption sites but precisely modulates the chemical environment within the MOF's pores. The decorated single-atom Zn(II) sites act as open metal sites with strong Lewis acidity, enabling potent electrostatic interactions with benzene's π electron cloud and enhancing benzene capture efficiency. MIL-125-defect and MIL-125-Zn were subjected to *In situ* FTIR spectroscopy to probe their structural evolution upon incremental benzene loading (Figure 5d,e). Following benzene adsorption, characteristic peaks associated with the Zn(II) sites exhibited shifts, which provided the evidence of the interaction between benzene and these metal centers. Through sophisticated defect engineering, conventional "structural defects" can be transformed into highly efficient adsorption sites. The Xu group prepared a quasi-MOF, quasi-Ni_8PBA, by controllably removing some ligands [101]. This material retains the basic framework of the parent MOF while creating a large number of unsaturated metal coordination sites (Figure 5f). Partial ligand removal exposes nickel sites previously occupied by ligands, transforming them into highly reactive unsaturated coordination sites. This structure enabled highly efficient electrooxidation of 5-hydroxymethylfurfural to 2,5-furandicarboxylic acid.

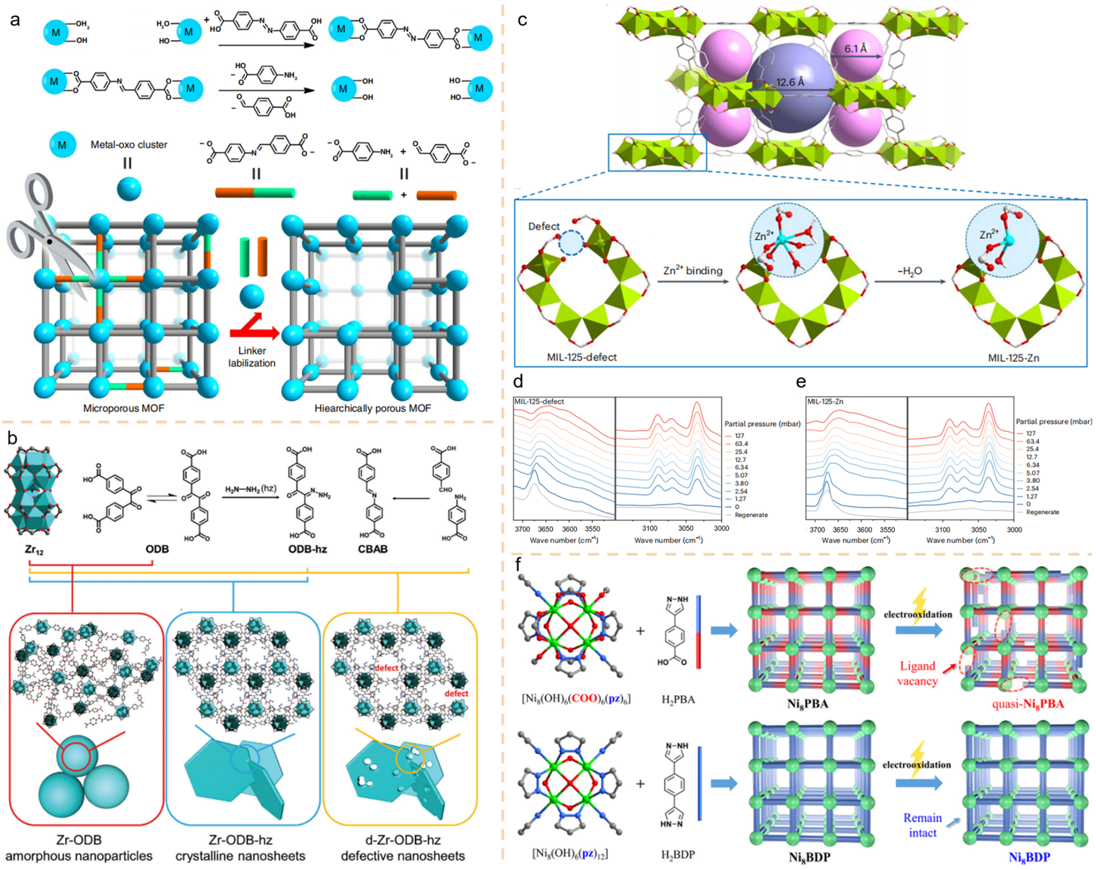

Figure 5. (**a**) Hierarchical porous MOF developed via ligand labilization [97]. Copyright 2017, Nature; (**b**) Schematic of dynamic-mediated strategy for synthesizing amorphous Zr-ODB nanoparticles [98]. Copyright 2024,

Wiley; (**c**) Schematic of a single atomic Zn(II) site modifying a defect in MIL-125; (**d**) *In situ* FTIR for MIL-125-defect; (**e**) *In situ* FTIR for MIL-125-Zn [100]. Copyright 2024, Nature; (**f**) Illustration of the synthetic routes and structures of quasi-Ni_8PBA and Ni_8BDP [101]. Copyright 2025, American Chemical Society.

2.2. Post-Synthesis Processing Method

The direct synthesis approach exhibits limitations in terms of functional group compatibility. Many functional groups sensitive to temperature, acidity/alkalinity, or solvents cannot withstand the reaction conditions required for one-pot synthesis. Consequently, when target functionality necessitates the introduction of such sensitive groups, post-synthesis modification strategies demonstrate their unique value.

Many of the functional groups—such as unstable reactive groups or large chiral groups—cannot withstand the high temperatures, strong acids/bases, or solvent conditions required for one-pot MOF synthesis [102,103]. Post-synthesis processing, which allows for the initial synthesis of a stable parent MOF bearing "reactive handles" (e.g., $-NH_2$, -OH, -CHO), enables the introduction of these sensitive groups under milder conditions.[104] The core concept of post-synthetic modification involves constructing the framework first, followed by the functionalization of its interior [66]. Based on a pre-synthesized MOF (referred to as the parent MOF), further chemical or physical treatments are applied to alter its chemical composition, pore environment, or surface properties without completely destroying its core crystal framework.

2.2.1. Self-Assembly

Self-assembly differs from the traditional one-pot method in that it emphasizes a stepwise, dynamic assembly process [105]. Rather than settling for the synthesis of a static framework, it focuses on developing a dynamic, intelligent "processing" technology that actively guides MOF materials toward their intended structure and function through stepwise operations or external stimuli [106]. Building higher-order macroscopic structures or materials using porous MOF nanoparticles as assembly units is a cutting-edge area in current MOF research [107]. Assembly-induced synthesis combines the multiple advantages of nanomaterials and porous materials: precise construction of multi-pore systems, high functional integration and tunability, flexibility in morphology and macroscopic structure, significantly enhanced stability, and mechanical properties [108–112].

Metal micro/nano-structured arrays have important applications in sensing, catalysis, metamaterials, and other fields [113,114]. Uniformly sized polystyrene or silica microspheres can self-assemble into structurally ordered monolayers (colloidal crystal templates), and combined with electrochemical, wet chemical, thermal evaporation, and other material growth methods, various micro/nano-structured arrays can be obtained. In this process, colloidal crystal templates function as masks or molds (Figure 6a). While traditional micro/nano fabrication methods can produce complex micro/nano structure arrays, they are time-consuming and costly. To achieve more complex micro/nano structure arrays, new functions of colloidal crystal templates must be developed. Yang et al. discovered a previously unidentified guided growth function of MOF templates, which can direct the electrochemical growth of metals under MOF templates, thereby forming nano-patterns identical to the metal surface (Figure 6b) [115]. They utilized gas/liquid interface self-assembly to prepare a single-layer film of UiO-66 octahedral particles, which features a large area and uniform structure (Figure 6c). The single-layer UiO-66 octahedra floating on the water surface display vibrant rainbow colors, indicating their ordered arrangement. This induced growth mode demonstrates strong universality, applicable to various MOF particle films and the electroplating of multiple metals.

Monodisperse colloidal inorganic nanoparticles (NPs) can form ordered superstructures through self-assembly. Compared with randomly stacked NPs, 2D superstructures can improve the exposure of reactants and accelerate mass transfer. The proposed aqueous colloidal ice template strategy successfully self-assembles MOF NPs into 2D quasi-ordered superstructures [116]. As shown in Figure 6d, the self-assembly process does not require any external fields. Monolayer and bilayer structures of MOF nanoparticles can be readily obtained through precise adjustment of their colloidal concentration. By rapidly freezing the MOF suspension in liquid N_2 and forming self-assembled superstructures through freeze-drying, monodisperse truncated rhombic dodecahedral ZIF-8 (TR-Z8) nanoparticles were synthesized. TR-Z8-1 NPs are stacked in an ordered manner within the self-assembled monolayer (Figure 6e). The prepared TR-Z8-2 exhibits a well-ordered bilayer structure (Figure 6f). The ice-template method can be extended to the preparation of superstructures for various MOFs.

In the context of green chemistry and future industrial applications, traditional solvent-thermal methods are energy-intensive, time-consuming, and difficult to scale up. The Jiang research group employed a low-energy synthesis strategy induced by seed crystals, introducing the same crystal nuclei of the target product to trigger surface growth during synthesis, thereby avoiding the high-energy nucleation stage and achieving MOF synthesis under mild conditions [117]. Taking Zr-based MOFs as an example, the researchers selected four representative structures—UiO-66, UiO-66-NH_2, MOF-808, and DUT-67—and first obtained seeds under solvothermal conditions at 100–120℃. These seeds were then introduced into the corresponding reaction systems at lower temperatures to facilitate crystal growth. The MOFs continued to grow epitaxially on the seeds, exhibiting a significantly higher growth rate compared to conventional low-temperature solvothermal synthesis (Figure 6g). MOFs synthesized at 50°C or even room temperature exhibit crystallinity and porosity comparable to those of the seeds, with porosity even exceeding that of MOFs synthesized under traditional solvothermal conditions. Traditional synthesis methods often struggle to achieve the controlled preparation of complex nanostructured single-crystal MOFs, particularly in terms of maintaining single-crystal properties while introducing multi-level pore structures and complex topological morphologies. Li’s team proposed a new method called “site-specific anisotropic assembly and etching co-mediation” [118]. This strategy breaks away from a conventional approach of relying solely on growth or etching, instead finely tuning the balance between the two to successfully synthesize a series of structurally intricate single-crystal MOF nanostructures, such as hexapods, nested nanocages, and octopods. Starting with ZIF-8 nanocubes, the researchers selectively grew mesoporous silica ($mSiO_2$) nanosheets on the {100} crystal faces of the ZIF-8 nanocubes while selectively etching the {100} crystal faces, thereby preliminarily constructing cube-shaped ZIF-8&$mSiO_2$ nanohybrids. By finely tuning the balance between growth and etching, the researchers successfully transformed the cubic hybrids into more complex hexapod hybrid structures. They then selectively removed the $mSiO_2$ layers via alkaline etching, yielding structurally complex and aesthetically pleasing single-crystal MOF nanoparticles (Figure 6h). This method allows for secondary epitaxial growth, enabling the construction of core-shell structures or multi-component heterojunctions. The resulting complex nanostructures successfully incorporate a multi-level pore system while maintaining single-crystal integrity. The single-crystal nature ensures the material’s excellent structural stability and ordered pores, while the multi-level pore system facilitates material transport and diffusion.

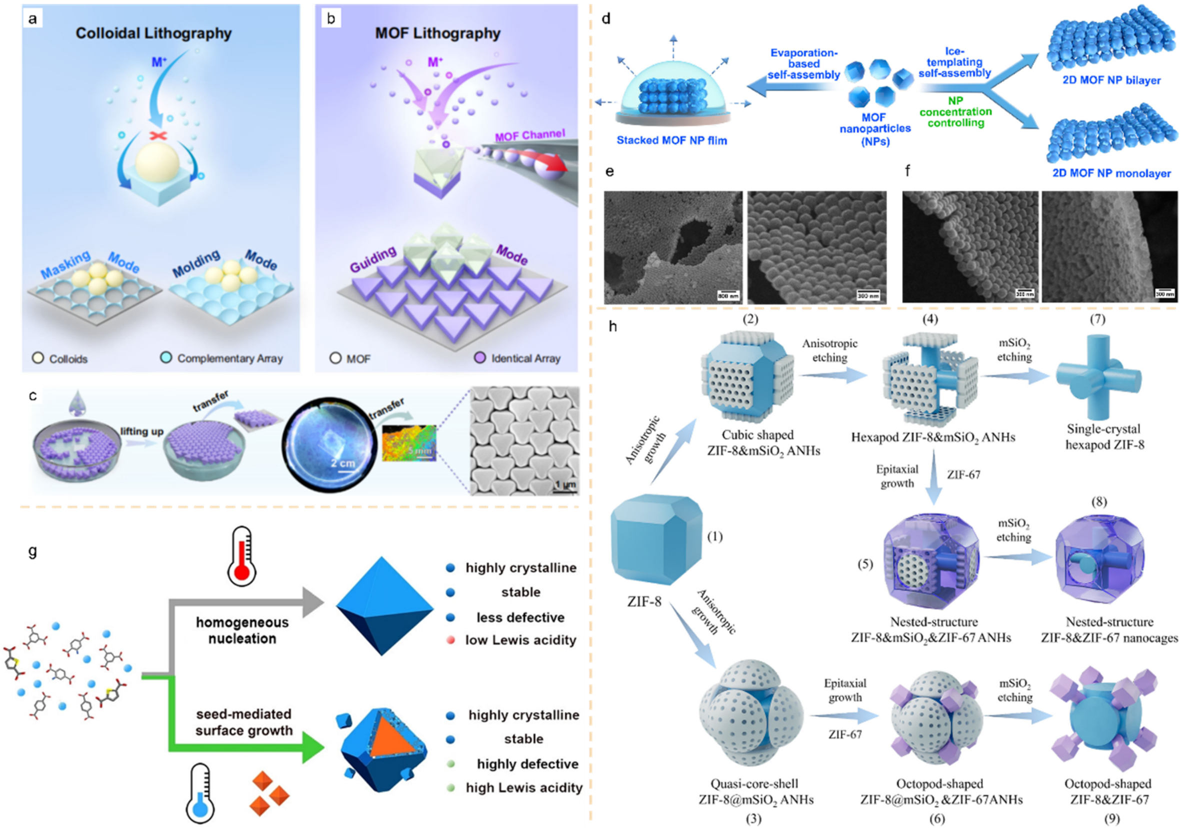

Figure 6. (**a**) Colloidal lithography mask and molding growth method. (**b**) Guided growth method of MOF lithography. (**c**) Assembly of UiO-66 octahedral particles at the gas/liquid interface [115]. Copyright 2023, Nature; (**d**) Schematic diagram of ice template self-assembly strategy for constructing mono- and bilayer MOF superstructures. (**e**) SEM images of TR-Z8-1 monolayer. (**f**) SEM images of TR-Z8-2 bilayer [116]. Copyright 2022, American Chemical Society. (**g**) Schematic diagram of crystal seed-induced MOF synthesis [117]. Copyright 2025, Wiley. (**h**) Evolution diagram of MOF nanohybrids and single-crystal MOFs [118]. Copyright 2025, Wiley.

2.2.2. Acid/Alkali Adjustment

The chemical action of acids or bases enables the controlled creation of defects, modification of pore structures, and even morphological transformations within MOFs [119–121].

The core principle of acid/alkali adjustment lies in exploiting the differing stability of various chemical bonds within the MOF framework toward acids or alkalis, selectively breaking specific bonds to achieve precise control over transitions from localized defects to overall structural transformations [122].

Acid adjustment primarily targets the metal-oxygen bonds within the metal-oxygen clusters [123]. The H^+ in acids compete with metal nodes in the MOF for coordination sites, protonating and coordinating with basic groups (such as carboxylate ions) bound to the metal and causing the weakening and breaking of metal-ligand coordination bonds [124]. The soft template method is an exciting candidate approach for constructing mesoporous MOFs owing to its attractive features of tunable mesoscopic structure and adjustable pore size [125]. By regulating the interfacial tension between surfactant micelles and MOF subunits through coordinate bonding, their controlled co-assembly can be achieved, thereby enabling the precise embedding of micelles within the MOF framework [126]. However, excessively strong interactions increase tension, leading to mismatches between crystallization process and the co-assembly of micelles with MOF framework building blocks [127].

In 2025, Li's group reported the synthesis of uniform single-crystal mesoporous MOF nanoparticles. Leveraging a synergistic acid-mediated assembly strategy, these nanoparticles feature well-ordered mesochannels embedded within a microporous framework [128]. HCl and CH_3COOH served as structural tension modulators to obtain the mesoporous UiO-66 (Figure 7a). This strategy operates by harmonizing structural forces across both the microscopic (MOF crystallization) and mesoscopic (micelle/MOF co-assembly) scales. This process allows precise control over MOF crystallization kinetics, synchronizing it with micelle assembly dynamics and MOF growth. Field-emission scanning electron microscopy (FESEM) characterization shows that the resulting nanoparticles exhibit uniform distribution and adopt a truncated octahedral crystal structure featuring eight hexagonal faces and six square faces (Figure 7b). The mesoporous structure, characterized by an ordered hexagonal arrangement, is clearly observable on the crystal faces. The HCl/CH_3COOH ratio in the assembly system offers precise control over the particle size of single-crystal mesoporous UiO-66. As HCl/CH_3COOH ratio increased from 4:6 to 8:2, the particle size exhibited a significant decrease trend from 1 μm to 45 nm (Figure7c). Powder X-ray diffraction (PXRD) patterns confirm the crystallinity and phase purity of the mesoporous MOFs, matching the simulated fcu-type UiO-66 structure. Diffraction peaks broadened with increasing HCl/CH_3COOH ratio, further indicating reduced particle size. Small-angle X-ray scattering (SAXS) patterns of meso-UiO-66 reveal that the two-dimensional hexagonal microstructure (*p6mm*) is also preserved.

They employed Avrami–Erofe'ev model to study the crystallization kinetics of single-crystal meso-UiO-66 nanoparticles (Figure 7d,e). When CH_3COOH was used alone, the MOF crystal precursor underwent a short 8-min induction period followed by extremely rapid crystallization (Figure 7f). Under these conditions, mesopores were not observable in the resulting MOF nanoparticles. Conversely, when HCl was used alone, the MOF crystallization process was nearly halted. The crystallization rate of single-crystal mesoporous UiO-66 decreased from 0.068 min^{-1} to 0.047 min^{-1} as the HCl/CH_3COOH ratio increased from 4:6 to 6:4. This was accompanied by a reduction in crystal diameter from ~1 μm to ~325 nm, while well-preserving the ordered mesophase. Further increasing the HCl/CH_3COOH ratio to 7:3 led to a shorter induction time (6 min), a slower crystallization rate (0.041 min^{-1}), and finer grains of ~105 nm. This indicates that both HCl and CH_3COOH are essential for the formation of mesoscopic UiO-66 in single crystals. Therefore, strong and weak acids jointly mediate a synergistic assembly mechanism for mesoscopic MOF formation in single crystals. CH_3COOH serves to control the framework crystallization rate, while HCl promotes the micelle-MOF co-assembly, thereby achieving a synergistic balance. (Figure 7g–i). Without HCl and CH_3COOH, the samples exhibit an amorphous state lacking ordered mesoscopic structures. Strong inorganic acids inhibit MOF subunit crystallization while promoting surfactant micelle assembly, whereas weak organic acids exert the opposite effect.

The primary targets of base adjustment are organic ligands, particularly those containing chemical bonds unstable toward bases. OH^- can attack and cleave ester bonds, amide bonds, and other functional groups within ligands, initiating nucleophilic substitution reactions. MOFs featuring open metal sites have emerged as promising catalysts due to their well-defined and protected active centers, yet the integration of highly polarized components like sulfide bridges or metal-sulfur clusters remains scarcely explored [129–131]. By utilizing the stable topology, extensive structural databases, and mild synthesis of pre-formed MOFs, post-synthetic modification enables precise alteration of bridging groups (Figure 8a) [132]. Xie et al. employed post-synthesis modification techniques to convert chlorine ligands into hydroxides, which were transformed into sulfide groups, thereby embedding metal-sulfur active sites within MOFs [133]. They selected a class of MOFs (M_2Cl_2BBTA, M = Co, Ni) featuring one-dimensional (1D) metal-chloride chain structures, where chlorides serve as bridging ligands, forming well-defined and easily replaceable bridging structures (Figure 8b). The conversion of chlorides to SH groups with hydrogen sulfide was slow and incomplete, hindered by the reversible equilibrium driven by the HCl byproduct.

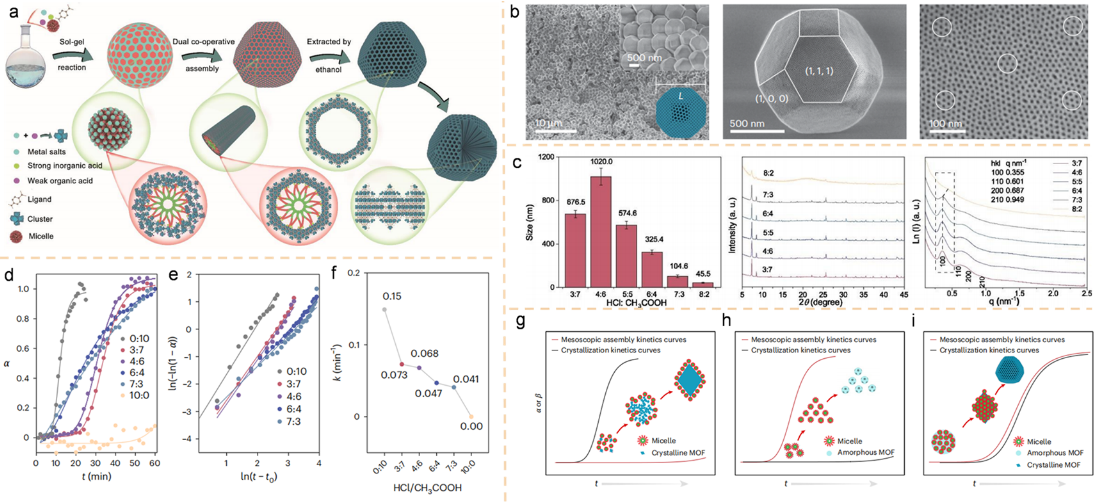

Figure 7. (**a**) Diagram of the synergistic assembly strategy using strong and weak acids for synthesizing single-crystal meso-MOFs. (**b**) FESEM characterization of meso-UiO-66 fabricated via cooperative strong/weak acid-mediated assembly. (**c**) Characterization of meso-UiO-66 synthesized with different ratio of HCl/CH_3COOH. (**d**) Crystallinity (α) as a function of reaction time for meso-UiO-66 nanoparticles synthesized at different HCl/CH_3COOH ratios. (**e**) The linear fitting of the crystallization kinetics curves. (**f**) Rate constant k at different HCl/CH_3COOH ratios. (**g**–**i**) Diagram of the microscopic (black, α) and mesoscopic (red, β) kinetic profiles for different HCl/CH_3COOH systems: (**g**) CH_3COOH only; (**h**) HCl only; and (**i**) their mixture, with α and β denoting crystallinity and mesoscopic orderliness, respectively [125]. Copyright 2025, Nature.

To overcome this limitation, the authors treated the chlorine-containing MOF with potassium hydroxide, converting bridging chloride anions into bridging hydroxyl groups. This yielded the resulting MOF product, named $M_2(OH)_2BBTA$ (Figure 8c). By employing *In situ* pair distribution function (PDF) data acquisition, the authors successfully achieved direct observation of the temporal evolution of the framework's local ordered structure. Local changes occurred almost immediately upon contact with high-concentration KOH solution (Figure 8d). The approximately 15-s delay observed after experiment initiation was attributed to dead volume in the sample environment upstream of the sample. The rapid conversion from Co_2Cl_2BBTA to $Co_2(OH)_2BBTA$ was further confirmed by ex situ PDF studies conducted using more dilute media. After five cycles of exposure to trace KOH, ligand exchange in the local ordering of metal nodes was observed through changes in peak intensity in the PDF data: the intensity of the Co–Cl bond peak diminished, while that of the Co–O bond peak increased (Figure 8e). The sulfidation process of $Co_2(OH)_2BBTA$ was initiated by *In situ* generation of H_2S using NaSH and acidified water as precursors, with the gas delivered to the sample via nitrogen carrier. Similar to the transition from Co–Cl to Co–OH species, local rearrangement at the metal center also occurred rapidly within minutes after gas flow reached the sample (Figure 8f). In the present study, the synthesis challenge of metal-sulfur MOFs was resolved, and the sulfur ligand-regulated electronic effects demonstrate universal applicability for developing highly efficient hydrogenation catalysts.

2.2.3. Thermal Solid-State Conversion

MOFs themselves are highly ordered porous crystals composed of metal nodes and organic linkers. When heated, their components and structures undergo a series of transformations [35,64,134,135]. Thermal solid-state conversion employs pre-engineered MOFs as "sacrificial templates" or "precursors". By precisely controlling heating temperature and duration, this post-synthesis modification strategy induces chemical conversion of the MOF precursor in the solid state, yielding new phase materials. This approach ingeniously leverages the structural and compositional design flexibility of MOFs to achieve precise "top-down" control over material morphology, composition, pore structure, and functionality. It enables the synthesis of novel functional materials that are difficult to produce via conventional solution-based methods.

Titanium metal-organic frameworks (Ti-MOFs) exhibit high stability and excellent optoelectronic properties, but their applications remain limited due to insufficient titanium content and a scarcity of accessible pores [136–138].

Since the discovery of the first Ti-MOF—MIL-91—in 2006, research in this area has been scarce, primarily because titanium chemistry in solution is difficult to control [139]. The reported Ti-MOFs all exhibit low condensation degrees (oxo/Ti ≤ 1), a key parameter in titanium chemistry for evaluating the properties of Ti–O compounds [140]. Higher ratios indicate that the Ti–O compound's properties approach those of TiO_2. Up to now, only a limited number of Ti–O cluster structures have been stably incorporated into MOF frameworks. Exploring new structural assembly strategies, particularly expanding the range of stable Ti cluster building blocks, has become crucial for advancing Ti-MOF development.

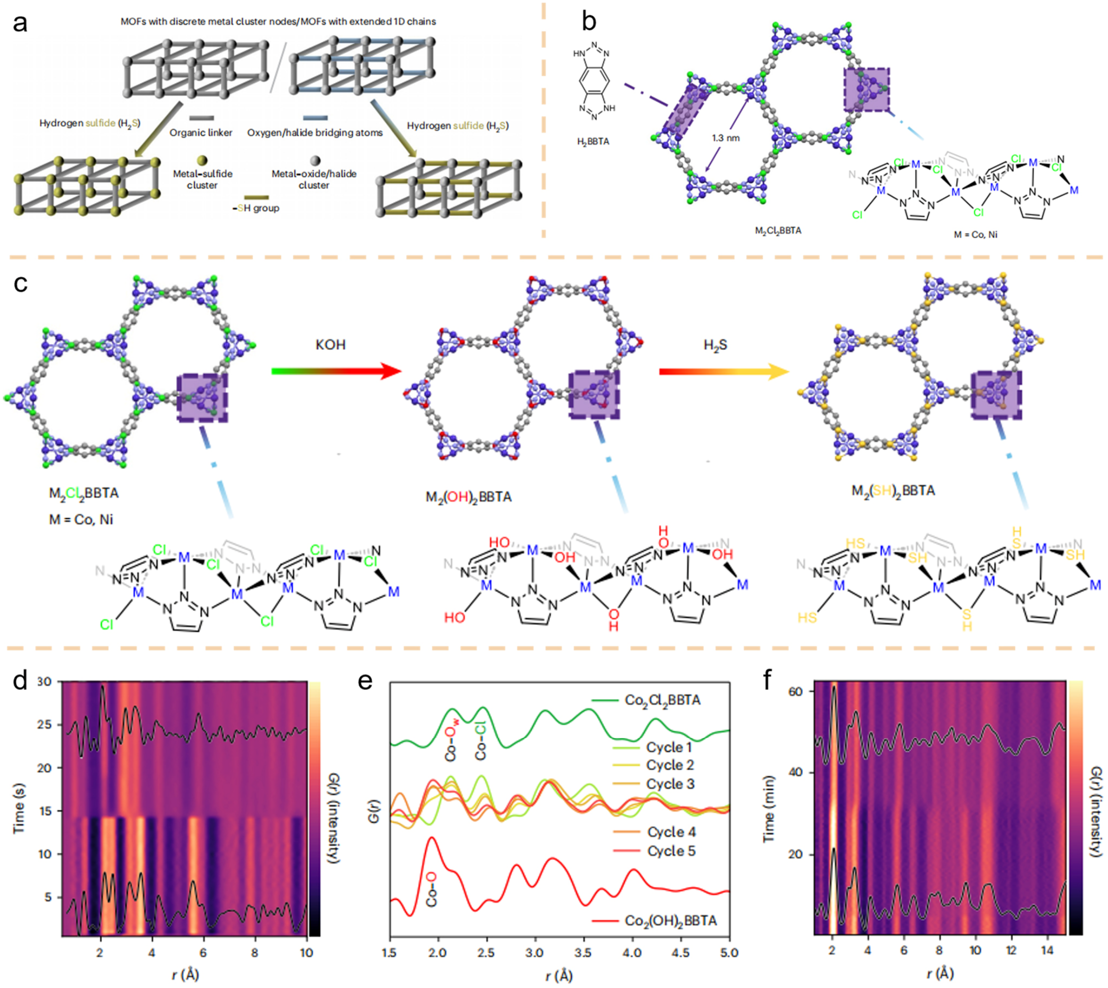

Figure 8. (**a**) Post-synthetic modification for attaching polarizable sulfur groups to MOFs. (**b**) M_2Cl_2BBTA with 1D metal chains. (**c**) Stepwise post-synthesis route for embedding metal-sulfur active sites in $M_2(SH)_2BBTA$. (**d**) Time-dependent PDF data of Co_2Cl_2BBTA under KOH flow. (**e**) PDF data of Co_2Cl_2BBTA before and after cycling with 0.1 M KOH. (**f**) *In situ* PDF data of $Co_2(OH)_2BBTA$ under H_2S flow [133]. Copyright 2025, Nature.

In 2018, Takashi Uemura et al. synthesized the 3D porous Ti-MOF (MIL-177-LT) via simple refluxing [141]. It exhibits exceptional stability under strongly acidic conditions. Moreover, MIL-177-LT undergoes a phase transition to the high-temperature form MIL-177-HT upon thermal induction, forming 1D infinite Ti–O subunits $(Ti_6O_9)_n$ with an unprecedented maximum condensation degree of 1.5 while retaining a highly crystalline porous structure (Figure 9a). MIL-177-LT irreversibly transforms into MIL-177-HT upon calcination at 280°C for 12 h (Figure 9b). MIL-177-LT comprises $Ti_{12}O_{15}$ cluster SBUs with a high condensation degree of 1.25, while MIL-177-HT achieves an unprecedented maximum condensation degree of 1.5 (Figure 9c,d). Following the irreversible thermal phase transition, all formic acid groups in the original structure are eliminated, and the Ti–O bond connections undergo an unusual rearrangement while retaining large hexagonal channels (Figure 9e). Subsequently, preliminary photoconductivity tests demonstrate that the one-dimensional infinite Ti-O nanowire SBUs in MIL-177-HT can produce photoconductivity comparable to that of bulk TiO_2.

MIL-125 stands as one of the most extensively studied representative structures among titanium-based MOFs due to its outstanding stability and photocatalytic performance. Constructed from $Ti_8O_8(OH)_4(OOC)_{12}$ clusters and terephthalic acid (BDC) ligands, MIL-125 exhibits a highly ordered crystalline topological structure [142,143].

However, the structural diversity of Ti-MOFs remains limited [144,145]. To date, only a small number of Ti-oxygen clusters have been stably incorporated into MOF frameworks, primarily due to the incompatibility between conventional solvothermal conditions and the stable coexistence of multiple Ti clusters [146,147]. Yuan team demonstrated a thermally solid-state synthesis strategy, utilizing the crystal-to-crystal transformation of MIL-125 and its functionalized derivatives to synthesize novel Ti-MOFs, named the MIL-125-R-HT (R = Naph, Br_2, Me_2, Anph, COOH, NH_2 or NO_2) series [148]. The phase transition temperature and crystallinity of MIL-125-R-HT are controlled by functional groups on the linkers, which influence the rotational flexibility required for cluster rearrangement and the thermal stability needed to prevent framework collapse (Figure 9f). Within the MIL-125-R-HT series, the naphthalene-functionalized variant (MIL-125-Naph-HT) exhibits the highest crystallinity. SEM images reveal that the pancake morphology of MIL-125-Naph (~1 μm) is well preserved after thermal treatment, indicating a crystal-to-crystal transition (Figure 9g). The high crystallinity maintained in MIL-125-Naph-HT enabled three-dimensional electron diffraction (3DED) data collection, yielding a crystal structure with a resolution of approximately 1.0 Å. The reconstructed 3D reciprocal lattice originates from two distinct crystals (Figure 9h). A key structural difference between the MIL-125-Naph and MIL-125-Naph-HT phases is the transformation of $Ti_8O_8(OH)_4(OOC)_{12}$ clusters into $Ti_8O_{10}(OOC)_{12}$ clusters. In the high-temperature phase, each $Ti_8O_{10}(OOC)_{12}$ cluster comprises four pairs of edge-shared TiO_6 octahedra connected via μ_2-O and μ_3-O bridges, forming a 12-fold connection node (Figure 9i). In MIL-125-Naph-HT, each Ti_8O_{10} core is bridged by 12 Naph linkers, forming a framework with an *fcu* topology (Figure 9j,k). The structural evolution of MIL-125-Naph during heating was monitored by *in situ* variable-temperature powder X-ray diffraction (VT-PXRD). Above 330°C, the diffraction pattern rapidly transformed into that characteristic of MIL-125-Naph-HT (Figure 9l). Between 290–330°C, broad, weak diffraction peaks were observed, attributed to the coexistence of different cluster types resulting from incomplete phase transformation and disruption of long-range order. After the transformation was completed above 330°C, the diffraction peaks re-sharpened, indicating the restoration of an ordered lattice (Figure 9m). The authors propose that this phase transition is driven by dehydration of hydroxyl groups within the $Ti_8O_8(OH)_4(OOC)_{12}$ clusters of MIL-125-Naph. To validate this hypothesis, thermogravimetric analysis coupled with mass spectrometry (TG-MS) was performed (Figure 9n). The MIL-125-Naph sample exhibited three distinct weight loss steps. A gradual 7.0% weight loss occurred between 200 and 400°C, accompanied by H_2O release. The mass spectrum revealed immediate CO_2 generation following H_2O release, indicating partial decarboxylation after dehydration. Consequently, the heat treatment temperature for synthesizing MIL-125-Naph-HT was controlled at 330°C to ensure complete phase transformation while avoiding linker degradation. This strategy successfully transformed the $Ti_8O_8(OH)_4(OOC)_{12}$ cluster into the $Ti_8O_{10}(OOC)_{12}$ cluster, previously reported only in discrete molecular clusters, achieving the first stable incorporation of this cluster structure into a MOF crystal.

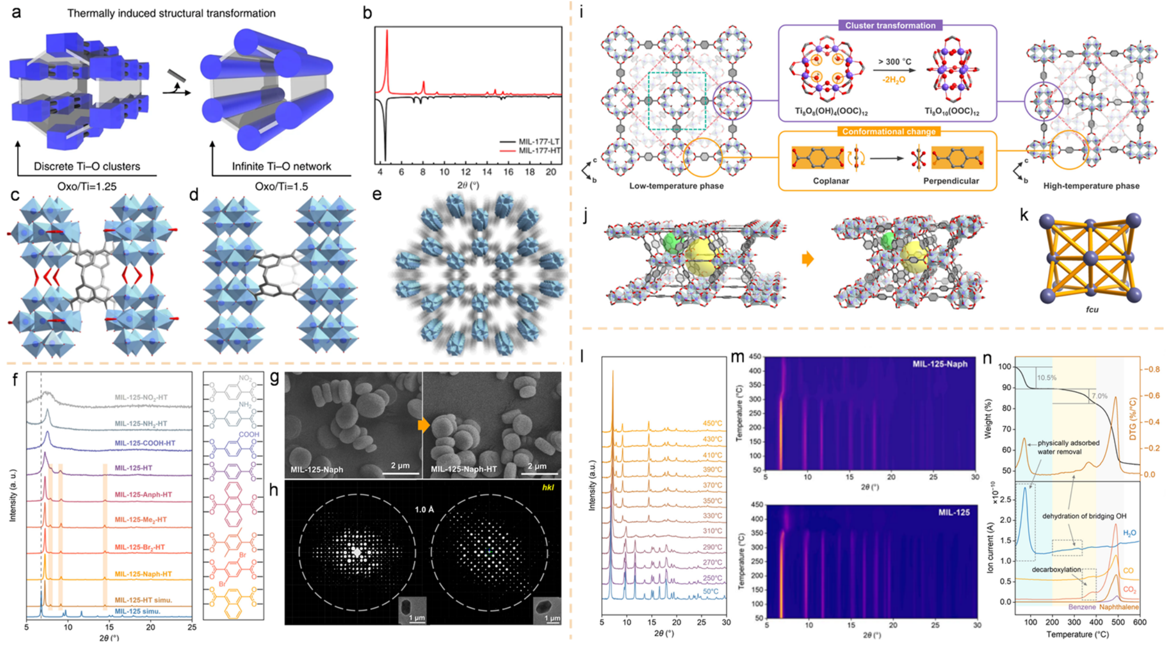

Figure 9. (**a**) Thermally induced structural transformation of MIL-177 MOFs; (**b**) PXRD comparison between MIL-177-LT and MIL-177-HT; (**c**) Adjacent $Ti_{12}O_{15}$ cluster SBUs with terminal and bridging formates (red) connected by ligands (gray); (**d**) Adjacent infinite ultrathin $(Ti_6O_9)_n$ nanowires with a thickness of 1 nm connected by ligands (gray); (**e**) Channels between the $(Ti_6O_9)_n$ nanowires array running along the *c*-axis with a diameter of

0.9 nm [141]. Copyright 2018, Nature; (**f**) PXRD patterns of relevant MIL-125 materials; (**g**) SEM images of MIL-125-Naph before and after thermal phase transition; (**h**) 3D reciprocal lattice of reflections in panel reconstructed from the 3DED data set of MIL-125-Naph-HT from two individual crystals; (**i**) Structural description of MIL-125-HT; (**j**) pores of MIL-125 and MIL-125-HT; (**k**) The *fcu* topological network of MIL-125-HT; (**l**) VT-PXRD patterns of MIL-125-Naph; (**m**) Stacked diffraction patterns and contour plot for MIL-125-Naph and MIL-125; (**n**) TG-MS curves of MIL-125-Naph [148]. Copyright 2025, American Chemical Society.

3. Catalytic Degradation of Waste Plastics by MOFs

The selective conversion of waste plastics into high-value organic compounds using catalytic technology to achieve resource utilization has become a research hotspot in recent years [149–151]. MOFs possess highly tunable crystalline structures, enabling precise design of pore dimensions, shapes, and surface chemistry. This facilitates selective adsorption and confinement of reactants, intermediates, and products, thereby providing an ideal microenvironment for specific catalytic reactions. Furthermore, MOFs interact with plastic polymer chains via their highly dispersed active sites, including Lewis acid sites, Brønsted acid sites, and metal-oxygen clusters [152–154]. Under mild reaction conditions, MOFs effectively activate C–C or C–O bonds [155,156]. Leveraging their structured pore confinement effects, they guide oriented cleavage of plastic molecules, converting them into high-value monomers, liquid fuels, or other chemicals [157,158].

However, when employing MOFs for catalytic reactions, their tolerance under various reaction media and conditions must be thoroughly evaluated—particularly their resistance to degradation behaviors like depolymerization. Enhancing the thermal stability, chemical stability, and hydrolytic stability of MOFs represents the current frontier and core challenge in this field [159,160]. Systematically evaluating MOF stability in catalytic environments not only aids in identifying the true catalytic active species but also determines whether the catalyst can achieve multiple cycles of reuse [120,161,162]. Should MOFs undergo ligand detachment, metal ion leaching, or framework disintegration during reactions, it becomes not only challenging to distinguish genuine active species but also impedes accurate comprehension of their catalytic mechanisms. This is crucial for advancing MOFs from fundamental research to practical applications.

3.1. Pyrolysis

Pyrolysis is a practical method for large-scale processing of mixed contaminated plastics, converting them into petrochemical products with industrial value [163,164]. Pyrolysis technology utilizes thermochemical reactions to degrade macromolecular plastic polymers into low-molecular-weight hydrocarbons under high-temperature conditions (350–900℃) in an oxygen-free or oxygen-deficient environment [165]. While acidic zeolites have long served as conventional catalysts for polyolefin pyrolysis, research on polymer catalysts—represented by MOFs—for promoting polymer depolymerization is gaining increasing attention [166,167]. MOFs exhibit higher porosity than zeolites and have been extensively studied as catalysts for forward polymerization reactions, suggesting untapped potential in depolymerization applications [168,169]. Compared to fully inorganic heterogeneous pyrolysis catalysts, the advantage of isoreticular synthesis strategies lies in their rational design capabilities for precisely tailoring catalytic active sites and pore sizes, thereby efficiently achieving targeted reaction activity [170].

In 2024, the Lim group demonstrated that UiO-66 with linker defects serves as an effective catalyst for polyolefin pyrolysis, enhancing liquid and gas product yields while suppressing undesirable char formation [171]. It is known that UiO-66 remains stable at 450°C, though this is below typical pyrolysis temperatures [159]. Yet, UiO-66 theoretically exhibits high reactivity, leading the research team to hypothesize that the reactivity of its unsaturated Zr nodes could lower the required pyrolysis temperature. The decomposition reaction of polyolefins occurs at the Lewis acidic Zr nodes without precious metal involvement (Figure 10a). The resulting products are aliphatic hydrocarbons, differing from the distribution of aromatic-rich hydrocarbon products generated by molecular sieve catalysis [172,173]. To evaluate the stability of the UiO-66 catalyst under pyrolysis conditions, researchers characterized the post-pyrolysis metal-organic framework residue using X-ray diffraction (XRD) and transmission electron microscopy (TEM). XRD analysis revealed that despite the presence of partially amorphous pyrolytic carbon residues, the characteristic diffraction peaks of UiO-66 remained clearly visible with only minor shifts (Figure 10b). No new peaks were observed, indicating no phase transition occurred. It is expected that polyethylene can enter the UiO-66 structure under similar conditions, given its larger pore window (6–7 Å) compared to the well-studied polyethylene pyrolysis catalyst HZSM-5 (5.5 Å) (Figure 10c).

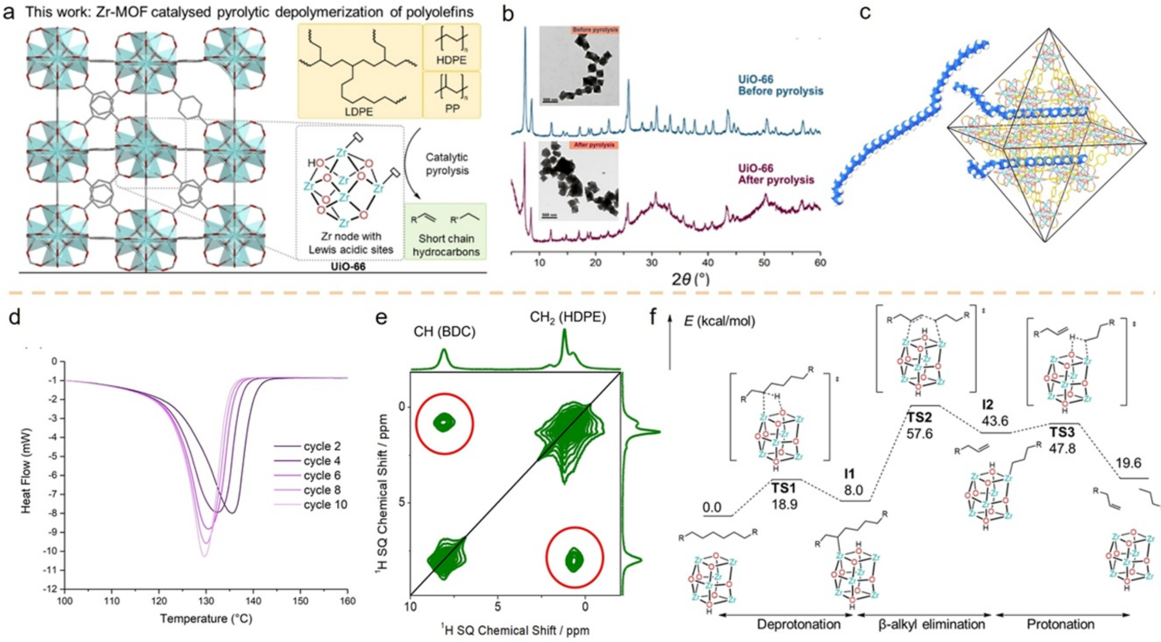

Figure 10. (**a**) UiO-66 with linker defects for pyrolysis of polyolefins; (**b**) XRD patterns and TEM images of UiO-66 before and after pyrolysis; (**c**) Illustration of HDPE strand infiltration into UiO-66 pore; (**d**) DSC thermogram of the UiO-66 mixture with HDPE; (**e**) ^{1}H 2D spin-exchange NMR spectrum (1H SQ/1H SQ homonuclear correlations) of UiO-66 and HDPE after heating to 350°C; (**f**) Modelled reaction profile illustrating the C–C bond cleavage catalyzed by unsaturated sites on a Zr atom [171]. Copyright 2024, Wiley.

To this end, the researchers first employed differential scanning calorimetry (DSC) to investigate polyethylene's ability to permeate into UiO-66 material under elevated temperatures. Since polymers confined within MOF pores do not contribute to the phase transition enthalpy of bulk polymers, the enthalpy measured per cycle indicates the amount of bulk polymer outside the MOF pores, thereby indirectly reflecting the amount of polymer entering the MOF pores. A physical mixture of activated UiO-66 and HDPE was heated to 200°C—sufficient to melt the polymer but well below its pyrolysis temperature—and held for 15 min to allow polymer penetration into the MOF (Figure 10d). Successive heating and cooling cycles of the UiO-66/HDPE system revealed a progressive reduction in the enthalpy changes of melting and crystallization. This evidence confirms the permeation of HDPE into the MOF framework upon melting. At temperatures closer to pyrolysis, the anticipated greater fluidity of the polymer and the flexibility of the UiO-66 framework prompted the team to employ a suite of solid-state NMR techniques to provide further evidence of polyolefin permeation into the MOF. After annealing a mixture of HDPE and UiO-66 for 2 h at 350°C under a nitrogen atmosphere, the ^{1}H 2D spin-exchange NMR (^{1}H SQ/^{1}H SQ homonuclear correlations) spectrum of the mixture clearly displayed a cross-peak, indicating intermolecular interactions between the polymer and MOF ligands (Figure 10e). DSC and solid-state 2D NMR studies indicate that polyolefins enter the pores of UiO-66 under pyrolysis conditions. This access allows the coordination-unsaturated nodes to act as catalytic sites while efficiently leveraging the material's extensive internal surface area. To validate the feasibility of their proposed mechanism, they employed *n*-decane as a polyethylene chain segment simulant and performed truncated cluster model calculations on the UiO-66. First, a zirconium alkyl complex is formed via a cooperative metallization-deprotonation process at a quaternary ring transition state (**TS1**). Subsequently, a low-energy bimetallic transition state (**TS2**) is reached, where adjacent Zr atoms at the node provide an empty coordination site. This transition state represents the rate-limiting step, yet remains slower than the rate of C–C bond cleavage. The reaction proceeds through **TS3**, restoring the zirconium moiety to its initial state and efficiently cleaving the starting alkane into a terminal alkene and a shorter alkane. Given that numerous MOFs exhibit thermal stability comparable to or exceeding that of UiO-66, coupled with pore sizes sufficient for polymer permeation, bottom-up MOF design offers multiple avenues for regulating pyrolytic reactivity and product selectivity. This study demonstrates the versatility of MOFs, which have been extensively studied for both ortho-polymerization and now effectively for depolymerization, opening new avenues for developing these multifunctional porous materials for waste plastic upgrading.

3.2. Hydrogenolysis

The technological approach of converting plastic waste into monomers or other high-value-added products has garnered significant attention in recent years, with its core objective being the realization of full-cycle recycling throughout the plastic lifecycle [174,175]. PET, serving as the primary raw material for manufacturing fibers, beverage bottles, and food packaging, has seen its global annual production exceed 70 million tons, making it a key focus for developing efficient recycling solutions [176]. Several common chemical processes for PET degradation, such as hydrolysis and alcoholysis, require substantial amounts of solvents and degradation agents, high reaction pressures, and the resulting oligomer byproducts are often difficult to separate [177–180]. The emergence of hydrogenolysis has thus become a more attractive strategy for deconstructing PET.

For industrial-scale catalytic processes, the most important performance parameters are the high conversion rate and high selectivity of the target product, as well as the high stability and reusability of the catalyst [181,182]. In catalyst development, amorphous catalysts often pose challenges for structural characterization due to their lack of long-range ordered structures, thereby limiting in-depth analysis of catalytic mechanisms [183,184]. In contrast, structurally defined crystalline catalysts typically feature uniformly distributed active sites. This not only facilitates revealing the essence of catalytic processes but also offers new avenues for enhancing catalytic efficiency and selectivity through structural design and active site regulation [185,186]. As star materials among coordination polymers in recent years, MOFs have demonstrated catalytic capabilities for hydrolysis, oxidation, and esterification reactions due to their Brønsted and Lewis acid sites at metal nodes [36,187–189]. UiO-66 within the Zr-MOFs family stands as one of the MOFs materials with the highest known thermochemical stability [190]. It not only exhibits high synthesis yields and large-scale production capabilities but also demonstrates significant potential for industrial applications, laying the foundation for its role as a potential industrial platform [191,192].

To thoroughly investigate whether Zr-MOFs can be used for deconstructing polyester plastics, the Farha team employed UiO-66 to conduct degradation reactions on waste PET plastic [193]. They mixed PET waste fragments (derived from plastic bottles) with 5 mol% UiO-66 powder in a vial and heated the mixture at 260°C under 1 atm H_2 for 24 h (Figure 11a). The collected transparent and green PET waste was directly exposed to UiO-66 without solvents. The products formed after the hydrogenolysis reaction sublimated and solidified at the top of the flask (Figure 11b). The products were confirmed as terephthalic acid (TA) and mono-methyl terephthalate (MMT) via ^1H and ^{13}C NMR spectroscopy (Figure 11c). PXRD analysis of the post-catalysis UiO-66 revealed that while the crystallinity of the sample was retained, significant changes occurred in peak positions and intensities. Two new peaks appeared at 7.45° and 8.74°, indicating partial structural alteration of the catalyst (Figure 11d). Previous studies by Guillerm et al. revealed that when zirconium salts react with TA, MIL-140A is the thermodynamic product, while the UiO-66 phase is the kinetic product [194]. Peak fitting analysis of the post-catalytic UiO-66 sample's PXRD pattern simultaneously identified characteristic peaks of both UiO-66 and MIL-140A. The nitrogen adsorption-desorption isotherm clearly showed a decrease in the specific surface area of the catalyzed UiO-66 (Figure 11e). SEM images reveal an alternative possibility: these images indicate a morphological change in the UiO-66 grains. Prior to the reaction, the grains exhibited an octahedral structure, which transformed into a rod-like morphology after catalysis—a morphology similar to that of MIL-140A (Figure 11f–h). Generally, esters and polyesters undergo thermal degradation via β-scission at elevated temperatures (Figure 11i). The higher yield observed under H_2 conditions suggests an alternative pathway, potentially involving hydrogenolysis, as reported in other studies [195].

Considering that the main reaction product TA is also an organic linker of UiO-66, they speculate that linker exchange may occur during degradation. To investigate this possibility, they performed PET degradation reactions using UiO-66-F and UiO-66-NH_2 (Figure 11j). These materials share the same zirconium-based node structure as UiO-66 but employ 2-fluoroterephthalic acid (TA-F) and 2-aminoterephthalic acid (TA-NH_2) as linking groups, respectively. ^1H NMR spectra revealed approximately 80% TA-F presence originating from UiO-66-F, indicating that during catalysis, the TA-F linker in UiO-66-F could be replaced by the PET degradation product TA. This process induces a phase transition in the MOF crystal, transforming it into MIL-140A. In contrast, UiO-66-NH_2 does not permit linker exchange with TA under identical conditions, retaining its original morphology and structure throughout the reaction. They speculate this linker transformation stems from differing acid dissociation constants (pKa) among the linkers. Linkers with higher pKa values form stronger linker-metal bonds within the MOF, making them more resistant to exchange [196]. TA, TA-F, and TA-NH_2 are 3.49, 2.86, and 3.95, respectively. This indicates that TA-F can be exchanged by TA, whereas exchanging TA-NH_2 with TA is significantly more challenging—particularly under conditions of extremely low substituent concentration.

Based on this, they propose a plausible reaction pathway for UiO-66-catalyzed degradation of PET (Figure 11k). First, UiO-66 catalyzes β-scission to generate intermediates 1 and 2. Next, intermediate 2 can undergo hydrogenolysis with H_2 to yield 1 and ethylene, or undergo hydrolysis in the presence of water in the system to yield 1 and acetaldehyde as the main products. Finally, intermediate 1 undergoes further decomposition via steps i, ii, and iii (main pathway) or via other side reactions during pyrolysis (minor pathway), ultimately forming TA and MMT. These discoveries reveal the multifunctional application characteristics of Zr-MOFs while also establishing the important position of MOFs as novel polymer degradation catalysts, thereby providing innovative solutions to tackle persistent challenges in plastic waste treatment.

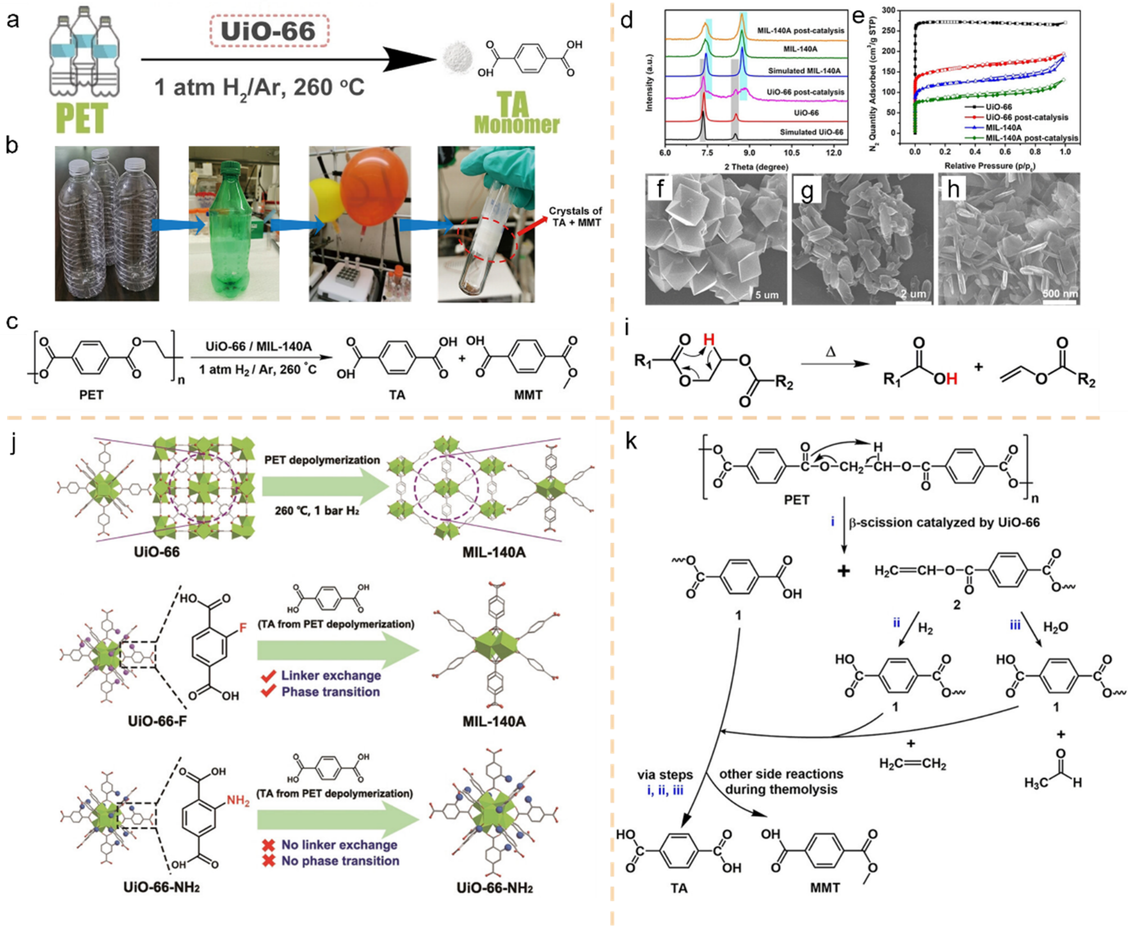

Figure 11. (**a**) Schematic diagram of UiO-66 catalytic degradation of PET; (**b**) The degradation process of discarded PET bottles; (**c**) Reaction formula for MOFs-catalyzed PET degradation; (**d**) PXRD patterns; (**e**) N_2 isotherms; (**f**) SEM image of UiO-66; (**g**) SEM image of UiO-66 post-catalysis under H_2 for 24 h; (**h**) SEM image of MIL-140A; (**i**) Thermolysis of polyesters via β-scission; (**j**) Illustration of structural phase transitions and linker exchange phenomenon in catalyst degradation processes; (**k**) Reaction mechanism of UiO-66 catalyzed degradation of PET [193]. Copyright 2022, Wiley.

3.3. Glycolysis

Glycolysis of waste plastics constitutes a chemical recycling method, specifically denoting the process whereby polyester plastics (such as PET) are decomposed into their monomers using ethylene glycol (EG) as both solvent and reactant under catalytic conditions [197,198]. With the characteristics of low reaction temperatures, mild conditions, stable yields, and scalability, the glycolytic method represents the most suitable process for decomposing PET at commercial scale [199]. For heterogeneous catalysts, achieving high-quality depolymerization into the *bis*(hydroxymethyl) terephthalate (BHET) remains challenging. This is primarily due to the low specific surface area of existing heterogeneous catalysts, which hinders the access of catalytic sites to the PET chains [200]. Consequently, this limitation restricts the overall activity of the glycolysis reaction. The emergence of MOF materials with large specific surface areas and high porosity holds promise for achieving highly efficient PET glycolysis reactions [201].

As early as 2017, Suo et al. pioneered the investigation of MOFs for PET degradation [202]. They synthesized three MOFs (ZIF-8, ZIF-67, and MOF-5), and the ZIF-8 with the largest specific surface area exhibited the strongest catalytic activity. Under ZIF-8 catalysis, PET pellets underwent complete depolymerization at 197℃

within 1.5 h, yielding BHET monomers as the primary product alongside minor dimer formation (Figure 12a). Thermal gravimetric analysis (TGA) of the three synthesized materials revealed excellent thermal stability across the glycolysis temperature range (160–200°C), with ZIF-8 exhibiting the highest thermal stability, as demonstrated in Figure 12b. Analysis of the NH_3- temperature programmed desorption (NH_3-TPD) curves revealed that ZIF-8 exhibited the strongest acidic sites, which facilitates the depolymerization of PET (Figure 12c). The high specific surface area and acidity of ZIF-8 account for its superior catalytic performance compared to ZIF-67 and MOF-5. Previous studies have investigated the catalytic activity of different metal ions during PET degradation. For instance, Ghaemy and Mossaddegh established an activity order for their catalysts as $Zn^{2+} > Mn^{2+} > Co^{2+} > Pb^{2+}$ [203].

However, owing to the relatively large size of the polymer chains compared to the micropores, PET polymer chains cannot penetrate the internal structure of ZIF-8 nanoparticles. This prevents the interfacial MOF-polymer active sites from catalyzing PET glycolysis. Consequently, the Lee team utilized triethylamine to synthesize dual-pore ZIF-8 (DPZIF-8) nanoparticles with mesoporous and microporous structures, thereby forming highly effective MOF-polymer catalytic reaction sites [204]. DPZIF-8 catalyzed PET glycolysis at 180°C for 4 h, achieving a PET conversion rate of 91.7% and a BHET yield of 76.1%—substantially higher than conventional ZIF-8 catalysts (Figure 12d). To address the PET conversion limitations of the large-pore MOF catalyst, Wu's team investigated metal azo salt framework-6 (MAF-6) in 2021 [205]. MAF-6 differs from ZIF-8 structurally by merely one methylene group in the imidazole ligand, yet its pore diameter (16.7 Å) is larger than that of ZIF-8 (11.6 Å) [206]. Moreover, the minimized energy of the degradation process allows dimer molecules to diffuse into MAF-6's pore structure (Figure 12e). The abundant active sites within this structure accelerate the reaction rate, achieving a maximum PET conversion of 92.4% and a BHET yield of 81.7%. MAF-6's larger pore size enables selective diffusion of dimers into the pores, where they are converted into BHET monomers. The corresponding degradation mechanism is subsequently proposed, as illustrated in Figure 12f. Zinc ions within MAF-6 act as Lewis acids, catalyzing successive ester exchange reactions. EG, functioning as a nucleophile, attacks the carbonyl carbon atom in PET via its hydroxyl oxygen, forming a transition state [207–209]. This further displaces the zinc ion, disrupting the ester bond in PET. Through continuous repetition of these reaction steps, oligomers and dimers are sequentially generated. Ultimately, the target monomer product BHET is formed.

To further overcome bottlenecks in the chemical recycling of polyester waste, Cao et al. proposed and validated an innovative catalytic strategy based on 'defect-engineered' MOF [210]. The research team ingeniously designed and synthesized a zinc-based MOF nanotube catalyst (*r*-Zn-MOF74-NT) rich in active sites, exploiting its ability to efficiently activate reaction mediators (EG and O_2) under mild conditions. The *r*-Zn-MOF74-NT was synthesized via a two-step process involving amorphous dissolution-recrystallisation-pyrolysis-reconstruction, as depicted in Figure 12g. The formation of Zn-MOF74 nanotubes (Zn-MOF74-NT) resulted from the partial dissolution of amorphous Zn-MOF74 in water. TEM characterization revealed the structural evolution of these nanomaterials across synthesis stages. The average size of Zn-MOF74-NT was approximately 1–5 μm, with the *r*-Zn–MOF74–NT structure comprising uniform nanoparticles (Figure 12h,i). The ESR spectrum in Figure 12j further confirms the ESR signal (g = 1.950) arising from zinc defects [211]. Compared to Zn-MOF74-NT, the *r*-Zn-MOF74-NT exhibits a significantly higher zinc defect concentration. *In situ* synchrotron infrared spectroscopy was employed to observe the temperature-dependent evolution of ethylene glycol's characteristic functional groups (Figure 12k). The catalyst and ethylene glycol were heated to 197°C for one hour within an infrared reaction cell. Notably, the characteristic peaks of ethylene glycol hydroxyl groups adsorbed on the catalyst surface (ν(C–OH) at 1101 and 1051 cm^{-1}), β(C–O–H) at 1402 cm^{-1} were markedly enhanced, indicating activation of the ethylene glycol hydroxyl groups [212]. The hydroxyl signals at 3384 and 3159 cm^{-1} gradually diminished, indicating that the primary hydroxyl groups in EG were activated by the r-Zn-MOF74-NT catalyst surface (Figure 12l). This peak intensity shift likely originates from the formation of O–H–Zn bonds, where hydroxyl groups directly interact with zinc sites on the *r*-Zn-MOF74-NT surface. This bonding phenomenon reveals strong interactions between EG and the catalyst, thereby effectively promoting EG activation in the glycolytic reaction. Combining *In situ* characterization, they delineated the glycolytic reaction pathway of PET on *r*-Zn-MOF74-NT into the following steps: (1) Ethylene glycol and oxygen molecules adsorb onto the r-Zn-MOF74-NT surface to form OOH* and $HOCH_2CH_2OH^*$; (2) Zinc vacancies within r-Zn-MOF74-NT activate the carbonyl oxygen of PET; (3) $HOCH_2CH_2OH^*$ undergoes a nucleophilic attack on the carbonyl carbon of PET. Synergistic catalysis facilitates the cleavage of PET's C–O bond, progressively generating BHET (Figure 12m). This study demonstrates that the *r*-Zn–MOF74–NT catalyst, rich in zinc defect sites, efficiently depolymerizes polyester waste into BHET. It is also scalable to different types of PET waste and other polyester materials, exhibiting strong activity and stability.

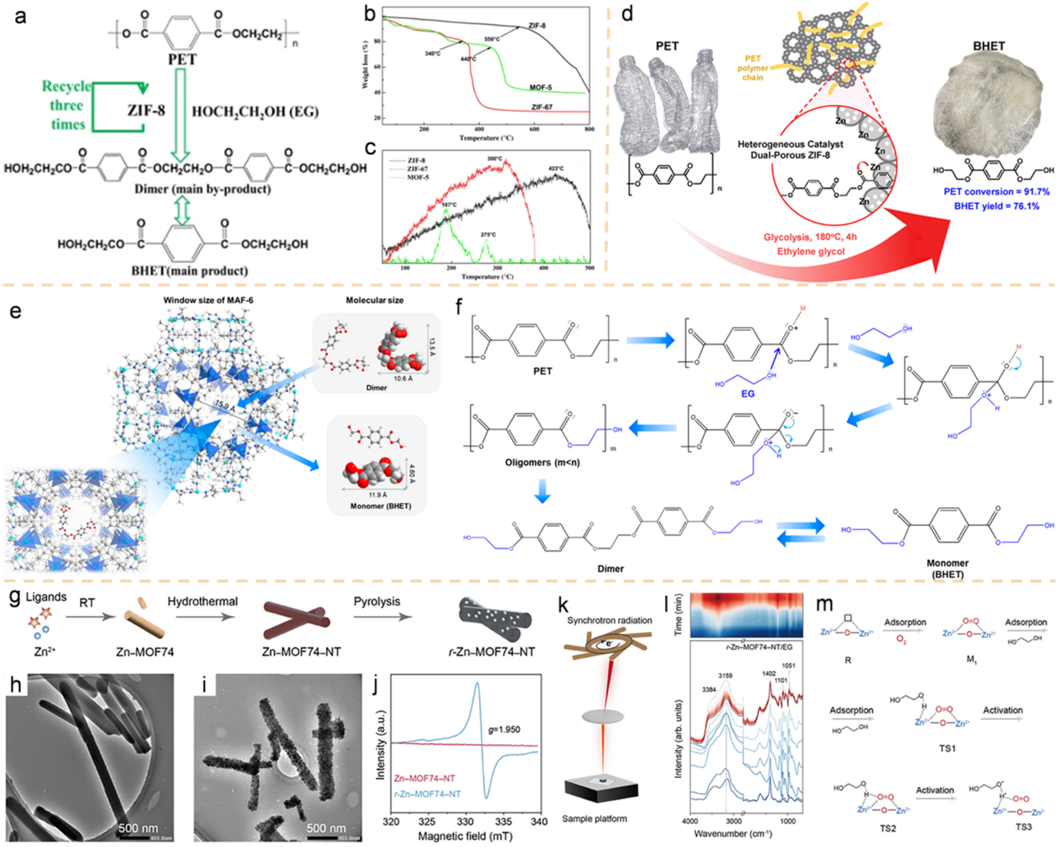

Figure 12. (**a**) Schematic illustration of ZIF-8-catalyzed glycolysis reaction of PET to BHET. (**b**) TGA curves. (**c**) NH_3-TPD curves [202]. Copyright 2017, Springer. (**d**) Schematic diagram of PET degradation by dual-porous ZIF-8 [204]. Copyright 2024, Elsevier. (**e**) Size of MAF-6 and of the Dimer and Monomer (BHET). (**f**) Proposed Reaction Mechanism for PET Glycolysis Catalyzed by MAF-6 [205]. Copyright 2021, American Chemical Society. (**g**) Schematic diagram of the synthesis of *r*-Zn–MOF74–NT. (**h**) TEM image of Zn-MOF74-NT. (**i**) TEM image of *r*-Zn–MOF74–NT. (**j**) ESR spectra. (**k**) Schematic illustration of *In situ* high-temperature infrared spectrometry. (**l**) *In situ* attenuated total reflectance (ATR) infrared spectra. (**m**) Schematic diagram of the atomic structure change of O_2 and EG on r-Zn–MOF74–NT [210]. Copyright 2025, Wiley.

3.4. Photocatalysis

Chemical upgrading recycling embraces the principle of "closed-loop recycling", not only transforming waste plastics into value-added raw materials but fundamentally providing a sustainable solution to plastic pollution [213,214]. Photocatalytic upgrading recycling technology, which utilizes solar energy to convert plastic waste into high-value products, has emerged as an attractive solution due to its operational simplicity and environmentally friendly characteristics [215]. To date, numerous photocatalysts—including TiO_2, g-C_3N_4, and Nb_2O_5—have been reported to convert plastic waste into fine chemicals [216–219]. However, the high energy barrier required for plastic chain scission remains a constraint on overall photocatalytic efficiency [22]. To enhance thermodynamic processes and advance the upgrading of plastic waste, the design and development of novel catalysts are imperative [220–222]. As a current star material, MOFs have drawn significant research attention. The metal nodes and organic ligands within MOFs can be precisely engineered and modulated like building blocks, thereby optimizing light absorption, band structure, and catalytic activity [60,223]. The regular and highly developed pore network within MOFs also provides abundant adsorption sites and reaction spaces for plastic molecules, facilitating thorough contact between reactants and active sites [224–226].

Inspired by hydrolytic PET enzymes yet overcoming their inherent limitations, the Dou research team proposed a nanozyme design strategy featuring asymmetric metal sites [227]. This nanozyme combines photocatalytic properties, enabling effective depolymerization of polyester plastics. Based on selected MOF catalysts, an asymmetric ligand substitution strategy was developed to construct defective MOFs with asymmetric sites (Figure 13a). Unlike MIL-101 synthesized solely from 2-aminoterephthalic acid, the defective D-MIL-101 incorporates both symmetric 2-aminoterephthalic acid and asymmetric benzoic acid in varying proportions during synthesis (Figure 13b). The differing electronic configurations and coordination environments of adjacent

$Fe^{3-\delta}/Fe^{3+}$ sites confer excellent catalytic activity upon the material. From the SEM images, the defect-bearing D-MIL-101 retains the pristine morphology of MIL-101, exhibiting a highly dispersed rhombohedral octahedral structure (Figure 13c). As shown in Figure 13d, photocatalytic degradation of various PET wastes using D-MIL-101 yields products comprising terephthalic acid (TPA) and ethylene glycol (EG). By adjusting the content of 2-aminoterephthalic acid and benzoic acid ligands, D-MIL-101 (60%) was ultimately determined to exhibit the optimal conversion rate. The yields of EG and TPA obtained using D-MIL-101 (60%) as a photocatalyst were higher than those achieved with MIL-101 and enzymes (Figure 13e). Comparison with other photocatalysts revealed that the optimized D-MIL-101 sample exhibited superior catalytic performance (Figure 13f). Adhering to a structure-function integrated design philosophy, the research team synergistically coupled the biomimetic catalysis of nanozymes with the photocatalytic properties of MOFs. This work not only pioneers a new direction for MOF catalyst structural design but also offers novel insights for the chemical recycling of polyester plastics.

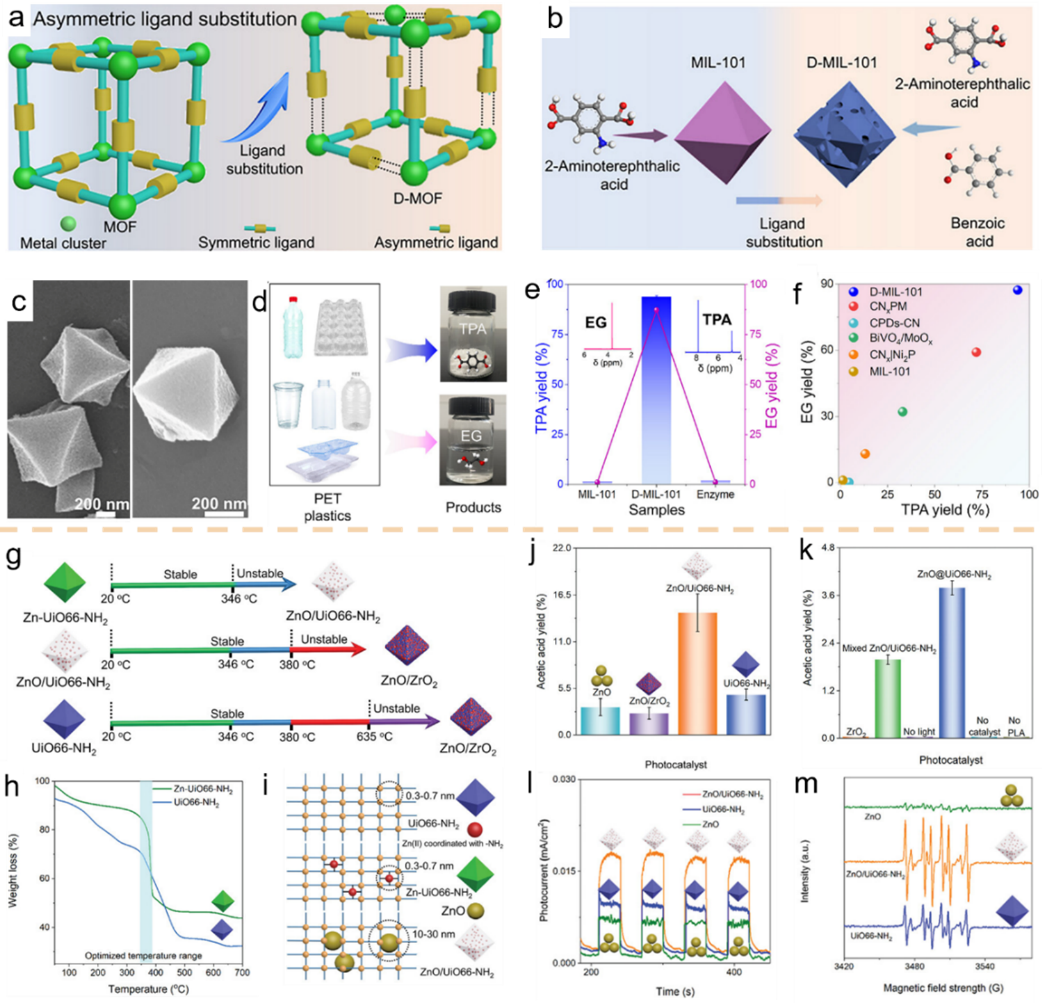

Figure 13. (**a**) Substitution strategy for asymmetric ligands. (**b**) Schematic diagram of the synthesis process incorporating 2-aminoterephthalic acid and benzoic acid to yield D-MIL-101. (**c**) SEM images of MIL-101 and D-MIL-101 (60%). (**d**) Recycling of discarded PET products. (**e**) Yields of TPA and EG in the enzyme, MIL-101 and D-MIL-101 (60%) reaction system. (**f**) Comparison of photocatalytic performance for PET degradation between D-MIL-101 (60%) and previously reported photocatalysts [227]. Copyright 2025, Wiley. (**g**) Calcination conversion temperatures of $UiO66\text{-}NH_2$, $Zn\text{-}UiO66\text{-}NH_2$, and $ZnO/UiO66\text{-}NH_2$, respectively. (**h**) TGA curves of $UiO66\text{-}NH_2$ and $Zn\text{-}UiO66\text{-}NH_2$. (**i**) Structural models of of $UiO66\text{-}NH_2$, $Zn\text{-}UiO66\text{-}NH_2$, and $ZnO/UiO66\text{-}NH_2$, respectively. (**j**) Acetic acid yield. (**k**) Acetic acid yield measured in the absence of light, photocatalyst, and PLA under various catalysts. (**l**) Transient photocurrent responses. (**m**) Transient photocurrent responses and electron spin resonance spectra of DMPO-$\bullet O_2^-$ [228]. Copyright 2023, Wiley.

Additionally, Dou's team had previously investigated the use of a partial calcination strategy to prepare heterojunction structures for the photocatalytic degradation of plastics [228]. TGA curve was first employed to study the calcination transformations of $UiO66\text{-}NH_2$ and $Zn\text{-}UiO66\text{-}NH_2$. As depicted in Figures 13g,h, the structure of Zn-UiO66-NH_2 becomes unstable beyond 346°C, with zinc sites undergoing *In situ* conversion to zinc oxide at this temperature, thereby forming a ZnO/UiO66-NH_2 heterojunction structure. This strategy preserves the framework structure of UiO66-NH_2, forming ultramicroscopic ZnO particles distributed within the skeleton. It altered the microporous structure of the MOF, generating mesopores within the ZnO/UiO66-NH_2 composite (Figure 13i). The prepared ZnO/UiO66-NH_2 simultaneously contains both micropores and mesopores (10–30 nm). Afterwards, they evaluated the photocatalytic activity of the prepared photocatalyst using polylactic acid (PLA) plastic as the target material. Compared to ZnO, Zn/ZrO_2, and UiO66-NH_2, the ZnO/UiO66-NH_2 heterojunction exhibited the highest acetic acid yield (Figure 13j). This indicates that the high specific surface area obtained at an appropriate calcination temperature is crucial for enhancing the catalytic activity of ZnO/UiO66-NH_2. To highlight the synergistic effects present in the ZnO/UiO66-NH_2 material during the upcycling of PLA, the research team conducted a series of control experiments (Figure 13k). They tested both physically blended ZnO/UiO66-NH_2 and the composite material ZnO/UiO66-NH_2, yet the acetate yield remained significantly lower than that of the heterojunction structure. This confirms that the strong bonding between zinc oxide and UiO66-NH_2 effectively enhances the photocatalytic conversion performance for plastic degradation. Control conditions involving light shielding and catalyst-free treatments confirmed that the photocatalytic degradation of PLA by ZnO/UiO66-NH_2 is light-driven. To elucidate the mechanism underpinning the enhanced catalytic activity of ZnO/UiO66-NH_2, they further investigated electron and hole separation efficiencies via photoelectrochemical measurements (Figure 13l). Among these photocatalysts, ZnO/UiO66-NH_2 exhibited the highest current density, indicating that embedding ultrafine ZnO particles within UiO66-NH_2 enhances electron-hole separation rates [229]. Electron spin resonance (ESR) spectra revealed the strongest $\cdot O_2^-$ signal peak intensity for the ZnO/UiO66-NH_2 photocatalyst (Figure 13m), indicating that embedding ZnO within UiO66-NH_2 pores enhances plastic conversion activity. This work provides a viable strategy for rationally designing heterojunction photocatalysts, while also offering insights into understanding the photocatalytic valorization process of plastics.

4. Adsorption of Microplastics by MOFs

Waste plastics remain persistent in the environment. In 2004, the concept of “microplastics” was first introduced in academic journals, specifically referring to plastic fragments smaller than 5 mm in diameter [230]. Within natural water bodies or soil environments, microplastics (MPs) are generated through natural processes such as degradation by ultraviolet light, mechanical fragmentation, and hydrolysis, originating from the breakdown of plastic products [231–234]. The presence of MPs in drinking water, foodstuffs and infant products has heightened concerns regarding adverse impacts on human health [235–237]. The key to tackling microplastic pollution lies in controlling its sources, a point that has gained global consensus [238,239]. However, source control often constitutes a protracted relay race, demanding sustained commitment across generations [240]. Against this backdrop, developing novel removal technologies may offer a more operationally feasible approach yielding short-term results [241].

Currently, MPs removal primarily relies on two technical approaches: adsorption and conversion [224]. Adsorption encompasses physical adsorption and filtration; conversion refers to transforming target pollutants into high-value-added chemicals through chemical or biological processes [242,243]. In recent years, adsorption techniques have gained recognition as an effective method for microplastic removal, owing to the development of adsorbents exhibiting strong affinity and high selectivity [244,245]. Micro-mechanism studies indicate that efficient removal is achieved through the combined action of multiple mechanisms between adsorbents and microplastics, including electrostatic adsorption, hydrogen bonding, π-π stacking, hydrophobic interactions, and complexation [246–249]. Against this backdrop, MOF materials demonstrate significant potential as ideal adsorbents [250]. Their structurally tunable nature enables synergistic adsorption of diverse pollutants through multiple mechanisms. These organo-inorganic hybrid materials possess controllable composition, structure, and morphology, facilitating material modification.

As a proof of concept, Xu’s team innovatively evaluated ZIF-67, achieving adsorption and removal of polystyrene microplastics (PS MPs, <10 μm) from water samples [251]. Considering ZIF-67’s stability, optimal adsorption conditions were established at pH 8.0 (Figure 14a). The results demonstrated that ZIF-67 exhibited favorable adsorption activity towards PS MPs, with an adsorption capacity of 34.5 mg g^{-1}. Further analysis indicated that hydrogen bonding interactions, π-π stacking, and electrostatic interactions played crucial roles in the adsorption of PS MPs by ZIF-67 in aqueous solutions [226,252,253]. To better investigate the interactions between functional groups and MP composition, Lan’s team selected melamine foam (MF) as an ideal substrate for loading stable Zr-MOFs. This approach was extended to various functional MOF systems (UiO-66-X, where X = H, NH_2, OH, Br, and NO_2) to study their microplastic removal performance [254]. MF, with its interpenetrating structure and numerous functional sites, provides an ideal platform for anchoring Zr-MOFs, ensuring rapid solvent passage and enabling thorough contact between microplastics and the framework (Figure 14b). Furthermore, the highly stable UiO-66-X is uniformly distributed across the MF framework, thereby demonstrating high contact potential for interactions between microplastics and MOFs. As observed in Figure 14c, five stable MOFs can be constructed by adjusting the ligand substituents of the Zr-MOF. To evaluate the potential of these foam materials for microplastic removal, the research team investigated their potential interactions by measuring the zeta potentials of different MOFs with microplastics. Measurements revealed that UiO-66-OH in Figure 14d exhibited a higher zeta potential than other MOFs, demonstrating strong interactions with microplastics. The prepared UiO-66-OH@MF material demonstrated higher removal efficiency for microplastics (Figure 14e). They confirmed that functional groups within Zr-MOFs further facilitated hydrogen bonding or van der Waals interactions with microplastics. The UiO-66-OH@MF material demonstrated the most effective microplastic removal, achieving an efficiency of 95.5 ± 1.2%.

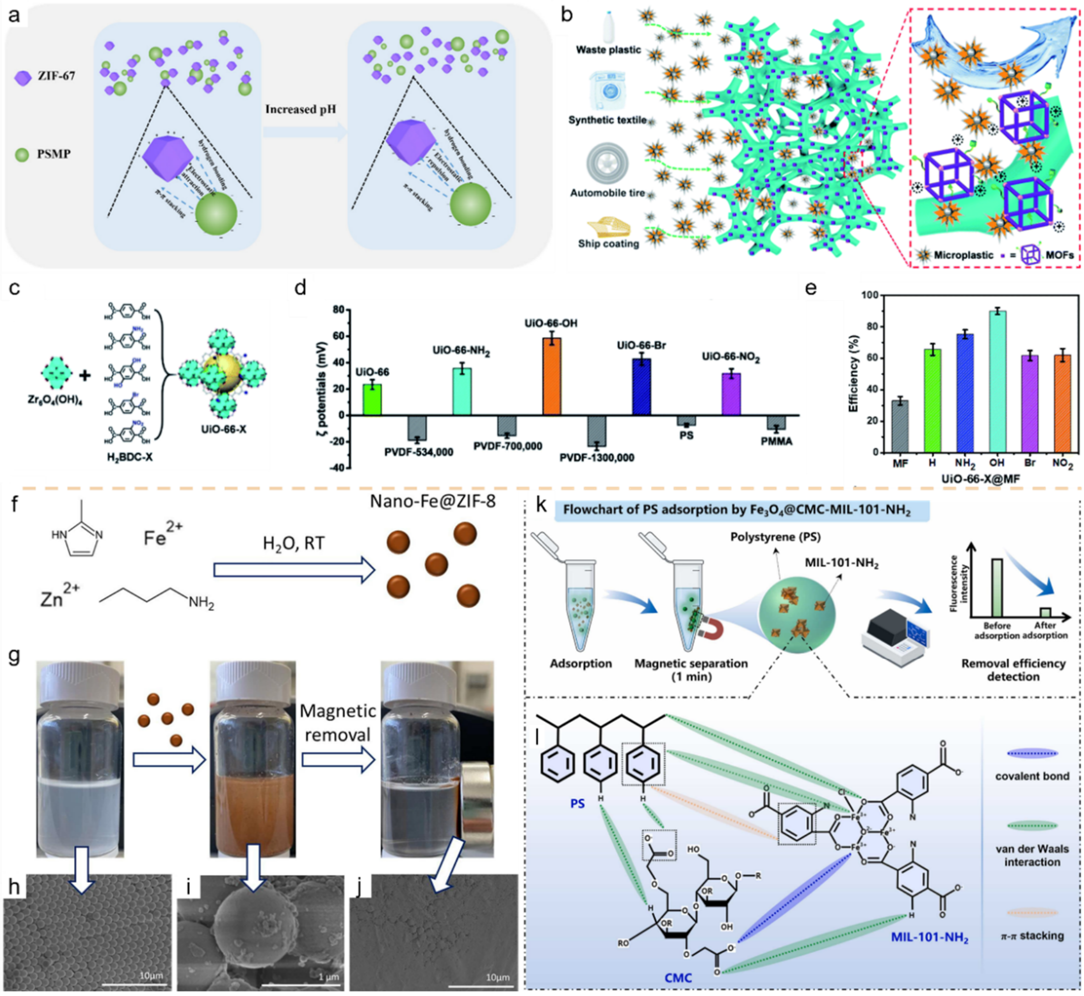

Figure 14. (**a**) Schematic diagram of ZIF-67 adsorption of PSMPs with increasing pH [251]. Copyright 2022, Multidisciplinary Digital Publishing Institute. (**b**) Schematic diagram of foam materials based on MOF for the removal of microplastics. (**c**) The structure of UiO-66-X (X = H, NH_2, OH, Br and NO_2). (**d**) The ζ potentials for various Zr-MOFs and microplastics. (**e**) The removal efficiency of UiO-66-X@MF [254]. Copyright 2020, Royal Society of Chemistry. (**f**) The preparation process of nano-Fe@ZIF-8. (**g**) A schematic diagram of using nano-Fe@ZIF-8 for magnetic extraction of microplastics. (**h**–**j**) The adsorption process of polystyrene microspheres as a model for microplastics [255]. Copyright 2022, Elsevier. (**k**) Flowchart of PS adsorption by Fe_3O_4@CMC-MIL-101-NH_2. (**l**) Schematic illustration of the interaction between CMC, MIL-101-NH_2 and PS [256]. Copyright 2025, Elsevier.

Beyond pure MOFs, MOF-based composites have recently emerged as adsorbents for removing emerging environmental pollutants. Maya’s team developed the first magnetic porous nanomaterial combining *n*-butylamine with inorganic modifiers (Figure 14f), synthesizing Nano-Fe@ZIF-8 via a room-temperature aqueous method [255]. Researchers evaluated the performance of this magnetic porous nanocomposite for removing microplastics and endocrine disrupting phenolic compounds from water samples (Figure 14g–j). The Nano-Fe@ZIF-8 nanoparticles achieved a removal efficiency of ≥98% for PS microspheres at a high concentration of 25 mg L-1 within 5 min. Given the characteristics of this magnetic removal process, the prepared material can also be used to extract and analyze MPs from environmental samples, thereby guiding future research directions. Chen et al. designed and synthesized engineered magnetic metal-organic frameworks (Fe_3O_4@carboxymethyl cellulose, CMC-MOFs) for adsorbing micro/nanoplastics, systematically investigating the structure-dependent adsorption behavior of the composite material towards microplastics [256]. Among these, Fe_3O_4@CMC-MIL-101-NH_2 demonstrated outstanding removal efficiency (98.0% achieved within 240 min) and adsorption capacity (240.6 mg g^{-1}). This magnetic structural design overcomes the limitations of conventional powdered MOFs, enabling rapid magnetic separation within one minute (Figure 14k). The remarkable properties of this composite are attributed to the combined action of its optimized framework and amino-functionalized surface. These dual characteristics act synergistically to enhance van der Waals interactions and π-π stacking (Figure 14l). By proposing a practical strategy to improve recyclability, this work not only advances the use of metal-organic frameworks for micro/nanoplastic remediation but also ensures their potential for high-value reuse in food purification processes.

5. Conclusions and Outlook

In summary, the unique structures, exceptional properties, and functional diversity of MOFs endow them with remarkable application potential, positioning these materials at the forefront of contemporary materials science research. Over the past decade, significant progress has been made in the design, synthesis, and mechanistic characterization of novel MOFs [257–259]. Against this backdrop, this review focuses on synthesis strategies, systematically analyzing the dominant roles of kinetic and thermodynamic parameters in MOF growth. It further reveals how these parameters, through the regulation of nucleation and growth steps, ultimately dictate key material characteristics such as pore size, structure, configuration, and crystallinity. The discussion comprehensively covers a wide range of preparation methods, from traditional to cutting-edge. The combination of porosity, high specific surface area, and easily accessible active sites makes MOFs promising catalysts, placing them at the forefront of research in waste plastic valorization and microplastic degradation in recent years [260].

Numerous studies have confirmed the outstanding efficacy of MOF-based catalysts—including pristine MOFs, composites, and their derivatives—across various catalytic processes such as thermal, photo-, and electrocatalysis [261,262]. These materials efficiently catalyze the depolymerization of waste plastics into valuable monomers, fine chemicals, or fuels, while also degrading microplastics into harmless products through the generation of highly reactive oxygen species [263]. The structural tunability of MOFs enables precise pore engineering and functionalization, allowing for the optimization of their catalytic activity, selectivity, and stability, thereby offering vast potential for the targeted conversion of plastic waste [171]. Through interdisciplinary innovation spanning chemistry, materials science, and engineering, MOF-based catalytic technology is poised to play a pivotal role in advancing the circular economy for plastics and building a sustainable society [264,265].

In the coming years, waste plastic recycling technology is expected to achieve a qualitative leap, manifested not only in enhanced processing efficiency but also through a fundamental innovation in the entire recycling model. The following key areas will provide the core driving force for this transformation (Figure 15).

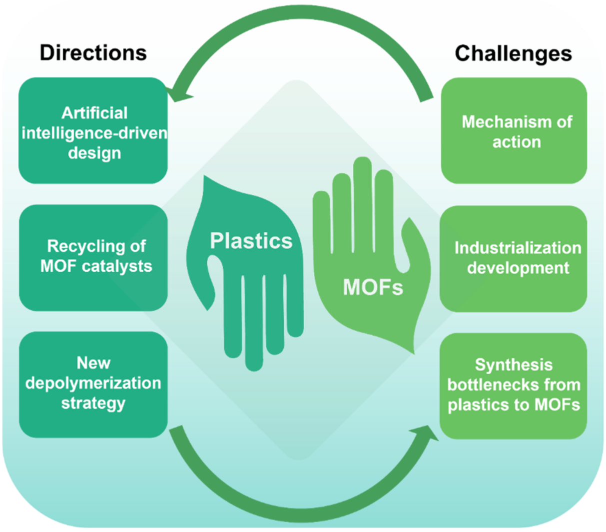

Figure 15. Schematic diagram illustrating the challenges and future development directions of MOFs as catalysts in waste plastic recycling.

5.1. AI-Driven High-Throughput Design and Structural Optimization

Achieving a paradigm shift from empirical exploration to rational design is crucial for the future of this field. The core pathway lies in the deep integration of artificial intelligence and high-throughput computational simulations. By leveraging machine learning models to thoroughly uncover the structure-property relationships, we can reversibly design novel MOF catalysts with tailored pore microenvironments, active sites, and stability. The ultimate goal of this research is to precisely align MOF structures with their functions, enabling the full-process optimization from selective adsorption to efficient catalytic cleavage of plastic macromolecules, thereby fundamentally enhancing reaction conversion efficiency and product selectivity.

5.2. Reusability and Stability Enhancement of MOF Catalysts

The long-term stability and economic feasibility of catalysts are fundamental prerequisites for their scaled application. Thermal stability is a critical prerequisite for the application of MOFs in various plastic thermal conversion processes, such as pyrolysis and gasification. Design strategies to enhance stability primarily focus on intrinsic structural reinforcement. The use of metal ions with high coordination bond strength serves as the foundation, while increasing the rigidity, aromaticity, and denticity of organic linkers can significantly strengthen the framework. Chemical stability, pertaining to the structural integrity of MOFs in aqueous, acidic, alkaline, and organic solvent environments, demands precise design tailored to specific reaction conditions. Introducing hydrophobic groups into the ligands or grafting hydrophobic molecules onto the pore surfaces through post-synthetic modification can substantially reduce water affinity within the pores, effectively inhibiting framework hydrolysis mediated by water. There is an urgent need to systematically investigate the deactivation mechanisms of MOFs under complex reaction conditions—such as active site poisoning, framework collapse, or pore blockage—and to develop efficient regeneration strategies based on mechanistic insights. Concurrently, it is essential to explore dynamically responsive MOF materials that undergo controlled "reconstruction" during catalysis to form more stable active structures. Alternatively, designing easily recoverable macroscopic configurations, such as magnetic composites or monolithic catalysts, can significantly improve the practical reusability of MOFs. These approaches represent critical pathways toward achieving sustainable operation of MOF-based catalytic systems.

5.3. Novel Depolymerization Strategies for Mixed Plastic Waste

Plastic waste in real-world scenarios is inherently complex and heterogeneous, making the development of robust catalytic systems capable of tolerating compositional diversity and impurity interference critically important. Key directions include: (1) designing MOF catalysts with selectivity toward specific polymers to enable the precise fractionation and sequential recovery of mixed plastics; and (2) developing novel coupled catalytic approaches, such as photo-thermal and electro-thermal processes, which leverage synergistic effects between different energy inputs to efficiently depolymerize mixed plastics under mild conditions. This will significantly reduce energy consumption and minimize undesirable side reactions.

By advancing research in these cross-disciplinary frontiers, MOF-based catalysts are poised to become a pivotal enabler of the closed-loop plastic economy, offering transformative solutions for the efficient valorization of plastic waste.

The path to deploying MOF catalysts in real-world plastic waste valorization and microplastic mitigation is paved with critical challenges.

5.4. Challenges in Elucidating the Mechanism of Action

A deep understanding of the interaction mechanisms between MOFs and microplastics is fundamental for optimizing catalyst design and enhancing degradation efficiency. However, current research is constrained by limitations in analytical techniques. Key microscopic processes remain unclear, including the adsorption behavior of microplastics on MOF pore surfaces and the interfacial catalytic reaction pathways—particularly in heterogeneous systems, such as the attack routes of reactive oxygen species and the chain-scission mechanisms of microplastics. Among these, the pore structure and particle size of MOFs serve as two pivotal material parameters that decisively influence catalytic performance, though the underlying mechanisms remain incompletely elucidated. Pore size directly impacts the mass transfer efficiency, adsorption capacity, and confinement effect of microplastic molecules or fragments within the channels, thereby regulating their contact probability with active sites. Meanwhile, the particle size of MOFs governs their physical contact efficiency with microplastic particles, dispersion properties, and the extent of active site exposure. To bridge this gap, a suite of advanced *In situ* characterization techniques must be developed and applied to monitor the dynamic MOF–microplastic interface in real time under relevant reaction conditions. This approach will allow for the precise correlation of the catalyst's pore structure and particle morphology with its macroscopic degradation performance, establishing clear structure–activity relationships to inform the rational design of high-performance catalysts. *In situ* X-ray absorption spectroscopy enables precise tracking of the evolution in electronic structure, coordination environment, and local geometry of metallic active centers within metal-organic frameworks during reaction processes. Neutron scattering and diffraction techniques, being highly sensitive to hydrogen atoms, are exceptionally well-suited for investigating the restricted motion and diffusion behavior of microplastic polymer segments within MOF channels, as well as the transport processes of reaction media such as water molecules. The synergistic application of these techniques will enable us to track reaction intermediates in real time, elucidate the dynamic evolution of active sites, and visualise interfacial processes.

5.5. Challenges in Scalability and Industrialization

The large-scale industrial application of MOF catalysts requires overcoming critical hurdles in reactor design and process control. Reactor Design: Most high-performance MOF catalysts (e.g., *r*-Zn-MOF74-NT nanotube catalysts for PET alcoholysis) have so far only been validated at the laboratory scale [210]. A major bottleneck lies in developing industrial-scale reactors that fully leverage the catalytic efficiency of MOFs while ensuring efficient mass/heat transfer and enabling continuous operation. This challenge is particularly pronounced for catalytic processes involving external energy inputs, such as light (photocatalysis) or electricity (electrocatalysis). Process Control and System Integration: The complexity of advanced catalytic systems demands precise control over reaction conditions. Furthermore, the integration of MOF-catalyzed units with upstream plastic waste pretreatment and downstream product separation/purification processes—coupled with the establishment of intelligent control systems—is essential to achieving economic viability for the overall technology.

5.6. Bottlenecks in MOF Synthesis from Waste Plastics

The direct utilization of waste plastics (including microplastics) as feedstocks for MOF synthesis represents an ideal pathway toward closed-loop plastic recycling. However, this approach faces challenges related to feedstock complexity and process sustainability. Additive Interference and Feedstock Adaptability: Real-world plastic waste contains complex additives—such as colorants, plasticizers, and stabilizers—that can occupy metal coordination sites, block pores, or introduce impurities during MOF synthesis. These interactions significantly compromise the crystallinity, porosity, and catalytic activity of the resulting MOFs. Carbon Emissions and Process-Wide Evaluation: While using waste plastics to synthesize MOFs is inherently a carbon mitigation strategy, the overall sustainability and economic feasibility of the process require systematic evaluation. It is essential to conduct rigorous life cycle assessment (LCA) and techno-economic analysis (TEA) to quantify the carbon emissions and environmental impacts across the entire value chain—from plastic waste collection to MOF synthesis and catalytic application. Comparative analyses with conventional disposal methods or alternative recycling technologies are needed to verify the genuine environmental and economic benefits of this route.

To conclude, the prospects for MOFs as depolymerization catalysts are broad. Their transition from fundamental research to commercial adoption is imperative and relies on a strategic partnership between academia and industry, a vital link for making scalable applications a reality.

Author Contributions

Y.S. (Yichun Su): conceptualization, methodology, software, writing—reviewing and editing, writing—reviewing and editing; Y.S. (Yuxin Shi): writing—reviewing and editing, investigation; L.J.: data curation; Y.L.: data curation; J.W.: visualization; H.Y.: writing—reviewing and editing; P.L.: supervision, writing—reviewing and editing. All authors have read and agreed to the published version of the manuscript.

Funding

This work was financially funded by the Jiangsu Province Engineering Research Center of Biodegradable Materials (KF2403), the Jiangsu Key Laboratory of Advanced Catalytic Materials and Technology (Grant No. BM2012110), Changzhou Longcheng Talent Programme—Foreign Talent Special Project (Grant No. CQ20254007), and the Jiangsu Province University Key Laboratory of High-end Chemicals Advanced Manufacturing. Support was also received from the Advanced Catalysis and Green Manufacturing Collaborative Innovation Center. Furthermore, funding from the Major Basic Research Project of the Natural Science Foundation of the Jiangsu Higher Education Institutions (23KJA530001) and the 'Qing Lan Project' of the Education Department of Jiangsu Province is gratefully acknowledged.

Institutional Review Board Statement

Not applicable.

Informed Consent Statement

Not applicable.

Data Availability Statement

We declare that we have no financial and personal relationship with other people or organizations that can inappropriately influence our work, and there is no professional or other personal interest of any nature or kind in any data, service, product and/or company that could be construed as influencing the position presented in the manuscript entitled.

Conflicts of Interest

The authors declare no conflict of interest.

Use of AI and AI-Assisted Technologies

No AI tools were utilized for this paper.

References

1. Lahive, C.W.; Dempsey, S.H.; Reiber, S.E.; et al. Acetolysis for Epoxy-Amine Carbon Fibre-Reinforced Polymer Recycling. *Nature* **2025**, *642*, 605–612.
2. Mao, Y.; Wang, P.; Cao, R.; et al. Catalytic Cascade Depolymerization for Sustainable Recycling of Waste Polyvinyl Chloride. *Nat. Sustain.* **2025**, *8*, 1513–1523.
3. Seo, H.; Hong, H.; Park, J.; et al. Landscape Profiling of PET Depolymerases Using a Natural Sequence Cluster Framework. *Science* **2025**, *387*, eadp5637.
4. Wang, H.S.; Agrachev, M.; Kim, H.; et al. Visible Light–Triggered Depolymerization of Commercial Polymethacrylates. *Science* **2025**, *387*, 874–880.
5. Chu, M.; Tu, W.; Zhang, Q.; et al. Co-recycling of Plastics and Other Waste Materials. *Nat. Rev. Clean Technol.* **2025**, *1*, 320–332.
6. de Witt, J.; Luthe, T.; Wiechert, J.; et al. Upcycling of Polyamides through Chemical Hydrolysis and Engineered *Pseudomonas putida*. *Nat. Microbiol.* **2025**, *10*, 667–680.
7. Ellis, L.D.; Rorrer, N.A.; Sullivan, K.P.; et al. Chemical and Biological Catalysis for Plastics Recycling and Upcycling. *Nat. Catal.* **2021**, *4*, 539–556.
8. Geyer, R.; Jambeck, J.R.; Law, K.L. Production, Use, and Fate of All Plastics Ever Made. *Sci. Adv.* **2017**, *3*, e1700782.
9. Wang, C.; Chu, H.; Wang, C. Converting Waste PET Plastics to High Value-Added MOFs-Based Functional Materials: A State of the Art Review. *Coord. Chem. Rev.* **2024**, *518*, 216106.
10. Jehanno, C.; Alty, J.W.; Roosen, M.; et al. Critical Advances and Future Opportunities in Upcycling Commodity Polymers. *Nature* **2022**, *603*, 803–814.
11. Conk, R.J.; Stahler, J.F.; Shi, J.X.; et al. Polyolefin Waste to Light Olefins with Ethylene and Base-Metal Heterogeneous Catalysts. *Science* **2024**, *385*, 1322–1327.
12. Liu, X.; Hu, Z.; Rettner, E.M.; et al. Catalytic Closed-Loop Recycling of Polyethylene-like Materials Produced by Acceptorless Dehydrogenative Polymerization of Bio-Derived Diols. *Nat. Chem.* **2025**, *17*, 500–506.
13. Nguyen, B.-N.T.; Tan, T.T.Y.; Otake, K.-I.; et al. MOF Catalysts for Plastic Depolymerization. *Angew. Chem. Int. Ed.* **2025**, *64*, e202504017.
14. Xing, C.; Mao, C.; Wang, S.; et al. Ambient Solar Thermal Catalysis for Polyolefin Upcycling Using Copper Encapsulated in Silicon Nanosheets and Chloroaluminate Ionic Liquid. *Nat. Catal.* **2025**, *8*, 556–568.
15. Tournier, V.; Duquesne, S.; Guillamot, F.; et al. Enzymes' Power for Plastics Degradation. *Chem. Rev.* **2023**, *123*, 5612–5701.
16. Ciccia, N.R.; Shi, J.X.; Pal, S.; et al. Diverse Functional Polyethylenes by Catalytic Amination. *Science* **2023**, *381*, 1433–1440.
17. Huang, X.; Li, Y.; Shu, Z.; et al. High-Efficiency Degradation of PET Plastics by Glutathione S-Transferase under Mild Conditions. *Environ. Sci. Technol.* **2024**, *58*, 13358–13369.

18. Lu, B.; Takahashi, K.; Zhou, J.; et al. Mild Catalytic Degradation of Crystalline Polyethylene Units in a Solid State Assisted by Carboxylic Acid Groups. *J. Am. Chem. Soc.* **2024**, *146*, 19599–19608.
19. Rahimi, A.; García, J.M. Chemical Recycling of Waste Plastics for New Materials Production. *Nat. Rev. Chem.* **2017**, *1*, 0046.
20. Lei, H.; Wang, Z.; Li, S.; et al. Recent Advancements in the Chemical Recycling and Biodegradation of Post-Consumer Polystyrene Waste. *Green Chem.* **2025**, *27*, 9357–9413.
21. Qin, J.; Wu, F.; Dou, Y.; et al. Advanced Catalysts for the Chemical Recycling of Plastic Waste. *Adv. Mater.* **2025**, *37*, 2418138.
22. Ran, H.; Sun, X.; Zheng, M.; et al. Synergistic Catalysis for Recycling and Upcycling of Plastics. *ACS Catal.* **2025**, *15*, 8551–8585.
23. Zhang, W.; Kim, S.; Wahl, L.; et al. Low-Temperature Upcycling of Polyolefins into Liquid Alkanes via Tandem Cracking-Alkylation. *Science* **2023**, *379*, 807–811.
24. Gao, Z.; Wang, Y.; Yuan, L.; et al. Room-Temperature Co-Upcycling of Polyvinyl Chloride and Polypropylene. *Nat. Sustain.* **2024**, *7*, 1691–1698.
25. Du, J.; Zeng, L.; Yan, T.; et al. Efficient Solvent- and Hydrogen-Free Upcycling of High-Density Polyethylene into Separable Cyclic Hydrocarbons. *Nat. Nanotechnol.* **2023**, *18*, 772–779.
26. Khopade, K.V.; Chikkali, S.H.; Barsu, N. Metal-Catalyzed Plastic Depolymerization. *Cell Rep. Phys. Sci.* **2023**, *4*, 101341.
27. Cen, Z.; Han, X.; Lin, L.; et al. Upcycling of Polyethylene to Gasoline through a Self-Supplied Hydrogen Strategy in a Layered Self-Pillared Zeolite. *Nat. Chem.* **2024**, *16*, 871–880.
28. Dong, Z.; Chen, W.; Xu, K.; et al. Understanding the Structure–Activity Relationships in Catalytic Conversion of Polyolefin Plastics by Zeolite-Based Catalysts: A Critical Review. *ACS Catal.* **2022**, *12*, 14882–14901.
29. Pingale, N.D.; Palekar, V.S.; Shukla, S.R. Glycolysis of Postconsumer Polyethylene Terephthalate Waste. *J. Appl. Polym. Sci.* **2010**, *115*, 249–254.
30. Wu, P.; Guo, M.; Zhang, R.-W.; et al. When Microplastics/Plastics Meet Metal–Organic Frameworks: Turning Threats into Opportunities. *Chem. Sci.* **2024**, *15*, 17781–17798.
31. Li, H.; Tipton, B.W.; Aboukeila, H.; et al. Upcycling of Waste Plastics into Carboxylic Acids for Biodegradable Surfactants. *Angew. Chem. Int. Ed.* **2025**, *137*, e202517471.
32. Gan, L.; Dong, Z.; Xu, H.; et al. Beyond Conventional Degradation: Catalytic Solutions for Polyolefin Upcycling. *CCS Chem.* **2024**, *6*, 313–333.
33. Wang, Y.; Liu, F.; Chen, J.; et al. Scale-Up Upcycling of Waste Polyethylene Terephthalate Plastics to Biodegradable Polyglycolic Acid Plastics. *Nat. Commun.* **2025**, *16*, 4440.
34. Yaghi, O.M.; O'Keeffe, M.; Ockwig, N.W.; et al. Reticular Synthesis and the Design of New Materials. *Nature* **2003**, *423*, 705–714.
35. Deng, S.; Xiong, Y.; Chen, C.; et al. Achieving Diverse CO_2 Conversions through On-Demand Installation of Multivariate Catalytic Sites into One Prototypical Metal–Organic Framework. *J. Am. Chem. Soc.* **2025**, *147*, 19996–20007.
36. Xu, Q.; Wang, X.; Liu, Y.; et al. Unlocking Precision in Biomass Conversion through Functional Ligand Engineering of Lewis Acidic MOFs. *Angew. Chem. Int. Ed.* **2025**, *64*, e202508256.
37. Wei, J.; Li, C.; Sun, Z.; et al. Nitrogen-Rich MOF-Material-Derived Metal Dual-Atom Platforms for Efficient Electrochemical Nitrate Reduction. *Angew. Chem. Int. Ed.* **2025**, *137*, e202517259.
38. Yu, Y.; Jiao, D.; Yi, L.; et al. Unique Electronic Regulation in Bimetallic MOF for Efficient Electrochemical Synthesis of H_2O_2 at 500 mA cm^{-2}. *Nano Energy* **2025**, *141*, 111096.
39. Zou, X.; Shi, Q.; Cheng, M.; et al. Metal–Organic Framework-Based Materials for Photocatalytic Hydrogen Peroxide Production: Insights into Mechanism, Modification Strategies, and Environmental Applications. *Adv. Energy Mater.* **2025**, *15*, 2501424.
40. Sun, N.; Shah, S.S.A.; Lin, Z.; et al. MOF-Based Electrocatalysts: An Overview from the Perspective of Structural Design. *Chem. Rev.* **2025**, *125*, 2703–2792.
41. Wang, H.; Yang, L.; Yang, Y.; et al. Multifunctional Bimetallic MOF Engineering: Innovative Synthesis and Versatile Applications in Adsorption, Catalysis, Sensing, and Energy. *Coord. Chem. Rev.* **2026**, *547*, 217114.
42. Su, Y.; Hu, J.; Yuan, G.; et al. Regulating Intramolecular Electron Transfer of Nickel-Based Coordinations through Ligand Engineering for Aqueous Batteries. *Adv. Mater.* **2023**, *35*, 2307003.
43. Baerlocher, C.; McCusker, L.B.; Olson, D.H.; et al. *Atlas of Zeolite Framework Types*, 6th ed.; Baerlocher, C., McCusker, L.B., Olson, D.H., Eds.; Elsevier Science B.V.: Amsterdam, The Netherlands, 2007; pp. 1–2. https://doi.org/10.1016/B978-044453064-6/50186-9.
44. Shu, L.; Peng, Y.; Song, H.; et al. Modular Customization and Regulation of Metal–Organic Frameworks for Efficient Membrane Separations. *Angew. Chem. Int. Ed.* **2023**, *62*, e202315057.
45. Yu, C.; Cen, X.; Zhang, Z.; et al. Step-Nucleation *In situ* Self-Repair to Prepare Rollable Large-Area Ultrathin MOF Membranes. *Adv. Mater.* **2023**, *35*, 2307013.

46. Gutiérrez, M.; Zhang, Y.; Tan, J. Confinement of Luminescent Guests in Metal–Organic Frameworks: Understanding Pathways from Synthesis and Multimodal Characterization to Potential Applications of LG@MOF Systems. *Chem. Rev.* **2022**, *122*, 10438–10483.
47. Li, C.; Chen, Z.; Sun, C.; et al. Topology-Tuned Structural Flexibility toward Customized Piezofluorochromism in Stable Zirconium MOFs. *Angew. Chem. Int. Ed.* **2025**, *137*, e16124.
48. Muralirajan, K.; Khan, I.S.; Garzon-Tovar, L.; et al. Ba/Ti MOF: A Versatile Heterogeneous Photoredox Catalyst for Visible-Light Metallaphotocatalysis. *Adv. Mater.* **2025**, *37*, 2405646.
49. Han, Z.; Yang, Y.; Rushlow, J.; et al. Development of the Design and Synthesis of Metal–Organic Frameworks (MOFs)—From Large Scale Attempts, Functional Oriented Modifications, to Artificial Intelligence (AI) Predictions. *Chem. Soc. Rev.* **2025**, *54*, 367–395.
50. Liang, R.; Fu, Y.; Han, Z.; et al. A Robust Pyrazolate Metal–Organic Framework for Integrated Perfluorooctanoic Acid Concentration and Degradation. *Nat. Water* **2024**, *2*, 1218–1225.
51. Hu, G.; Liu, Q.; Deng, H. Space Exploration of Metal–Organic Frameworks in the Mesopore Regime. *Acc. Chem. Res.* **2025**, *58*, 73–86.
52. Moghadam, P.Z.; Chung, Y.G.; Snurr, R.Q. Progress toward the Computational Discovery of New Metal–Organic Framework Adsorbents for Energy Applications. *Nat. Energy* **2024**, *9*, 121–133.
53. Greed, S.; Yaghi, O.M. The Man of MOFs and More. *Nat. Rev. Chem.* **2025**, *9*, 135–137.
54. Artsiusheuski, M.A.; Casati, N.P.M.; Clark, A.H.; et al. Controlling the Mechanism of Nucleation and Growth Enables Synthesis of UiO-66 Metal–Organic Framework with Desired Macroscopic Properties. *Angew. Chem. Int. Ed.* **2025**, *64*, e202415919.
55. Li, Q.; Zhang, Y.; Guo, X.; et al. Nucleation and Growth Mechanisms of Micro/Nano Structural Manganese-Trimesic Acid Coordinations for Aqueous Zinc-Ion Batteries. *Angew. Chem. Int. Ed.* **2025**, *64*, e202509741.
56. Cleeton, C.; Sarkisov, L. Inverse Design of Metal-Organic Frameworks Using Deep Dreaming Approaches. *Nat. Commun.* **2025**, *16*, 4806.
57. Han, Z.; Wang, K.-Y.; Liang, R.-R.; et al. Modular Construction of Multivariate Metal–Organic Frameworks for Luminescent Sensing. *J. Am. Chem. Soc.* **2025**, *147*, 3866–3873.
58. Snyder, B.E.R.; Turkiewicz, A.B.; Furukawa, H.; et al. A Ligand Insertion Mechanism for Cooperative NH_3 Capture in Metal–Organic Frameworks. *Nature* **2023**, *613*, 287–291.
59. O'Shaughnessy, M.; Glover, J.; Hafizi, R.; et al. Porous Isoreticular Non-Metal Organic Frameworks. *Nature* **2024**, *630*, 102–108.
60. Liu, B.; Wu, Y.; Wang, L.; et al. Covalent Organic Frameworks as Infinite Building Units for Metal–Organic Frameworks with Compartmentalized Pores. *Nat. Chem.* **2025**, *18*, 164–172.
61. Jin, H.; Zhao, P.; Qian, Y.; et al. Metal–Organic Frameworks for Organic Transformations by Photocatalysis and Photothermal Catalysis. *Chem. Soc. Rev.* **2024**, *53*, 9378–9418.
62. Wang, W.; Chen, D.; Li, F.; et al. Metal-Organic-Framework-Based Materials as Platforms for Energy Applications. *Chem* **2024**, *10*, 86–133.
63. Lin, Z.; Richardson, J.J.; Zhou, J.; et al. Direct Synthesis of Amorphous Coordination Polymers and Metal–Organic Frameworks. *Nat. Rev. Chem.* **2023**, *7*, 273–286.
64. Wu, K.; Zhao, W.; Huang, L.; et al. Aqueous-Phase Synthesis of Cyclic Trinuclear Cluster-Based Metal–Organic Frameworks. *J. Am. Chem. Soc.* **2025**, *147*, 13711–13720.
65. Liu, C.; Wang, J.; Wan, J.; et al. MOF-on-MOF Hybrids: Synthesis and Applications. *Coord. Chem. Rev.* **2021**, *432*, 213743.
66. Chen, W.; Ma, B.; Zou, R. Rational Design and Controlled Synthesis of MOF-Derived Single-Atom Catalysts. *Acc. Mater. Res.* **2025**, *6*, 210–220.
67. Huang, G.; Ma, J.; Chen, J.; et al. Controllable Strategy of Metal–Organic Framework Structural Stability: Regulation of Ligand Electronegativity by Esterification. *Adv. Sci.* **2025**, *12*, 2413853.
68. Song, B.; Song, W.; Liang, Y.; et al. Direct Synthesis of Topology-Controlled BODIPY and CO_2-Based Zirconium Metal-Organic Frameworks for Efficient Photocatalytic CO_2 Reduction. *Angew. Chem. Int. Ed.* **2025**, *64*, e202421248.
69. Zhang, W.; Wu, X.; Peng, X.; et al. Solution Processable Metal–Organic Frameworks: Synthesis Strategy and Applications. *Adv. Mater.* **2025**, *37*, 2412708.
70. Zhang, P.; Kang, X.; Tao, L.; et al. A New Route for the Rapid Synthesis of Metal–Organic Frameworks at Room Temperature. *CCS Chem.* **2023**, *5*, 1462–1469.
71. Chen, X.; Zhang, X.; Leng, C.; et al. Helical Polymer Metal–Organic Framework Hybrids. *Nat. Synth.* **2025**, *5*, 46–54. https://doi.org/10.1038/s44160-025-00909-1.
72. Koley, P.; Shit, S.C.; Yoshida, T.; et al. Metal Organic Framework Derived In_2O_3/ZrO_2 Heterojunctions with Interfacial Oxygen Vacancies for Highly Selective CO_2-to-Methanol Hydrogenation. *Nat. Commun.* **2025**, *16*, 8903.

73. Zeng, M.; Li, J.; Fan, S.; et al. Internally Extended Growth of Hierarchical MOF-on-MOF Nanostructures for Adsorption. *ACS Appl. Nano Mater.* **2025**, *8*, 11437–11446.
74. Cai, Z.; Xia, Y.; Ito, Y.; et al. General Synthesis of MOF Nanotubes via Hydrogen-Bonded Organic Frameworks toward Efficient Hydrogen Evolution Electrocatalysts. *ACS Nano* **2022**, *16*, 20851–20864.
75. Wang, J.; Jiang, Y.; Zhu, F.; et al. Design and Assembly of Continuous Macro-Micro-Porous Metal-Organic Framework Film Assisted by Atomic Layer Deposition for Biosensing. *Adv. Funct. Mater.* **2025**, *35*, 2419775.
76. Yuan, A.; Du, J.; Zheng, Y.; et al. Construction of 2D CoFe-MOF Derived from LDH Electrocatalyst for Efficient Oxygen and Urea Evolution. *J. Colloid Interface Sci.* **2025**, *684*, 243–250.
77. Xu, H.; Han, J.; Zhao, B.; et al. A Facile Dual-Template-Directed Successive Assembly Approach to Hollow Multi-Shell Mesoporous Metal–Organic Framework Particles. *Nat. Commun.* **2023**, *14*, 8062.
78. Shen, K.; Zhang, L.; Chen, X.; et al. Ordered Macro-Microporous Metal-Organic Framework Single Crystals. *Science* **2018**, *359*, 206–210.
79. Guo, Y.; Feng, L.; Wu, C.; et al. Confined Pyrolysis Transformation of ZIF-8 to Hierarchically Ordered Porous Zn-N-C Nanoreactor for Efficient CO_2 Photoconversion under Mild Conditions. *J. Catal.* **2020**, *390*, 213–223.
80. Yao, W.; Hu, A.; Ding, J.; et al. Hierarchically Ordered Macro–Mesoporous Electrocatalyst with Hydrophilic Surface for Efficient Oxygen Reduction Reaction. *Adv. Mater.* **2023**, *35*, 2301894.
81. Shen, L.; Zhang, X.; He, H.; et al. Template-Assisted *In situ* Synthesis of Superaerophobic Bimetallic MOF Composites with Tunable Morphology for Boosted Oxygen Evolution Reaction. *J. Colloid Interface Sci.* **2024**, *676*, 238–248.
82. Zou, Z.; Du, Z.; Dai, L.; et al. A Universal Approach for High-Yield Synthesis of Single-Crystalline Ordered Macro-Microporous Metal–Organic Frameworks. *J. Am. Chem. Soc.* **2024**, *146*, 31186–31197.
83. Liang, T.-W.; Chen, C.; Kusaka, S.; et al. Mesoporous Metal–Organic Framework from Templated Synthesis as Mechanical Metamaterials. *J. Am. Chem. Soc.* **2025**, *147*, 23608–23616.
84. Inagaki, S.; Guan, S.; Ohsuna, T.; et al. An Ordered Mesoporous Organosilica Hybrid Material with a Crystal-Like Wall Structure. *Nature* **2002**, *416*, 304–307.
85. Liu, T.; Zhao, Y.; Song, M.; et al. Ordered Macro–Microporous Single Crystals of Covalent Organic Frameworks with Efficient Sorption of Iodine. *J. Am. Chem. Soc.* **2023**, *145*, 2544–2552.
86. Xiao, Y.; Chen, Y.; Wang, W.; et al. Simultaneous Control of Flexibility and Rigidity in Pore-Space-Partitioned Metal–Organic Frameworks. *J. Am. Chem. Soc.* **2023**, *145*, 10980–10986.
87. Huang, C.; Sun, W.; Jin, Y.; et al. A General Synthesis of Nanostructured Conductive Metal–Organic Frameworks from Insulating MOF Precursors for Supercapacitors and Chemiresistive Sensors. *Angew. Chem. Int. Ed.* **2024**, *63*, e202313591.
88. Zhao, Z.; Zhao, Y.; Lin, R.; et al. Modular Super-Assembly of Hierarchical Superstructures from Monomicelle Building Blocks. *Sci. Adv.* **2022**, *8*, eabo0283.
89. Lv, Z.; Liu, M.; Yang, Y.; et al. Hierarchical Engineering of Single-Crystalline Mesoporous Metal–Organic Frameworks with Hollow Structures. *J. Am. Chem. Soc.* **2025**, *147*, 14585–14594.
90. Wang, X.; Zhang, S.; Li, M.; et al. Tailored Design of Mesoporous Metal Organic Framework Single Crystals by Kinetics-Mediated Micelle Assembly for Efficient Asymmetrical Single-Atom Catalysis. *Adv. Mater.* **2025**, *37*, 2500370.
91. Wu, T.; Chen, G.; Han, J.; et al. Construction of Three-Dimensional Dendritic Hierarchically Porous Metal–Organic Framework Nanoarchitectures via Noncentrosymmetric Pore–Induced Anisotropic Assembly. *J. Am. Chem. Soc.* **2023**, *145*, 16498–16507.
92. Yu, L.; Li, S.; Zhou, X.; et al. Building Ultramicroporous Zirconium Metal–Organic Frameworks with Ligands of High Coordination Density through a Reticular Approach. *Nat. Chem.* **2025**, *17*, 1207–1215.
93. Miao, J.; Ullah, S.; Sun, X.; et al. Constructing Alkali Metal–Organic Frameworks with High Porosity Utilizing a High-Connectivity Organic Linker. *J. Am. Chem. Soc.* **2025**, *147*, 26926–26933.
94. Yang, J.; Zhang, Z.; Jiang, Y.; et al. Net-Coded Organic Building Blocks for the Reticular Assembly of High-Connectivity Metal–Organic Frameworks. *J. Am. Chem. Soc.* **2025**, *147*, 20218–20224.
95. Shi, L.; Zhong, Y.; Cao, H.; et al. A Hetero-Supermolecular-Building-Block Strategy for the Assembly of Porous (3,12,24)-Connected Uru Metal–Organic Frameworks. *Nat. Synth.* **2024**, *3*, 1560–1566.
96. Yuan, S.; Chen, Y.-P.; Qin, J.-S.; et al. Linker Installation: Engineering Pore Environment with Precisely Placed Functionalities in Zirconium MOFs. *J. Am. Chem. Soc.* **2016**, *138*, 8912–8919.
97. Yuan, S.; Zou, L.; Qin, J.; et al. Construction of Hierarchically Porous Metal–Organic Frameworks through Linker Labilization. *Nat. Commun.* **2017**, *8*, 15356.
98. Li, Z.; Yao, B.; Cheng, C.; et al. Versatile Structural Engineering of Metal–Organic Frameworks Enabling Switchable Catalytic Selectivity. *Adv. Mater.* **2024**, *36*, 2308427.
99. Fonseca, J.; Meng, L.; Imaz, I.; et al. Self-Assembly of Colloidal Metal–Organic Framework (MOF) Particles. *Chem. Soc. Rev.* **2023**, *52*, 2528–2543.

100. Han, Y.; Huang, W.; He, M.; et al. Trace Benzene Capture by Decoration of Structural Defects in Metal–Organic Framework Materials. *Nat. Mater.* **2024**, *23*, 1531–1538.
101. Huang, N.; Chu, B.; Chen, D.; et al. Rational Design of a Quasi-Metal–Organic Framework by Ligand Engineering for Efficient Biomass Upgrading. *J. Am. Chem. Soc.* **2025**, *147*, 8832–8840.
102. Chen, T.; Li, H.; Shi, X.; et al. Robust Homochiral Polycrystalline Metal–Organic Framework Membranes for High-Performance Enantioselective Separation. *J. Am. Chem. Soc.* **2024**, *146*, 14433–14438.
103. Xie, S.; Tan, X.; Xue, Z.; et al. Cathodic Deposition-Assisted Synthesis of Thin Glass MOF Films for High-Performance Gas Separations. *Angew. Chem. Int. Ed.* **2024**, *63*, e202401817.
104. Mandal, S.; Natarajan, S.; Mani, P.; et al. Post-Synthetic Modification of Metal–Organic Frameworks toward Applications. *Adv. Funct. Mater.* **2021**, *31*, 2006291.
105. Ouyang, J.; Tao, H.; Yang, Z.; et al. Modulator Engineering of Bifunctional Metal-Organic Framework for Synergistic Catalysis. *Chem Catal.* **2025**, *5*, 101155.
106. Biswas, A.; Lemcoff, N.; Shelonchik, O.; et al. Molecular Light-to-Heat Conversion Promotes Orthogonal Synthesis and Assembly of Metal-Organic Frameworks. *Nat. Commun.* **2025**, *16*, 2758.
107. Zeng, L.; Huang, L.; Wang, Z.; et al. Self-Assembled Metal–Organic Framework Stabilized Organic Cocrystals for Biological Phototherapy. *Angew. Chem. Int. Ed.* **2021**, *60*, 23569–23573.
108. Huang, H.; Li, J.; Yuan, M.; et al. Large-Scale Self-Assembly of MOFs Colloidosomes for Bubble-Propelled Micromotors and Stirring-Free Environmental Remediation. *Angew. Chem. Int. Ed.* **2022**, *61*, e202211163.
109. Lyu, D.; Xu, W.; Payong, J.E.L.; et al. Low-Dimensional Assemblies of Metal-Organic Framework Particles and Mutually Coordinated Anisotropy. *Nat. Commun.* **2022**, *13*, 3980.
110. Ji, Y.; Lin, Y.; Qiao, Y. Interfacial Assembly of Biomimetic MOF-Based Porous Membranes on Coacervates to Build Complex Protocells and Prototissues. *Nat. Chem.* **2025**, *17*, 986–996.
111. Li, Z.; He, M.; Wang, Y.; et al. Advances in Biocompatible Metal-Organic Frameworks for Biomedical Applications. *Adv. Mater.* **2025**, *37*, 2503946.
112. Wu, X.; Gao, Y.; Wang, H.; et al. Hydrophobized Metal–Organic Frameworks as Versatile Building Blocks for Tailored Nanocrystal Superlattices. *J. Am. Chem. Soc.* **2025**, *147*, 6361–6366.
113. Ayata, M.; Fedoryshyn, Y.; Heni, W.; et al. High-Speed Plasmonic Modulator in a Single Metal Layer. *Science* **2017**, *358*, 630–632.
114. Balaur, E.; O' Toole, S.; Spurling, A.J.; et al. Colorimetric Histology Using Plasmonically Active Microscope Slides. *Nature* **2021**, *598*, 65–71.
115. Lu, Y.; Zhang, X.; Zhao, L.; et al. Metal-Organic Framework Template-Guided Electrochemical Lithography on Substrates for SERS Sensing Applications. *Nat. Commun.* **2023**, *14*, 5860.
116. Song, Y.; Song, X.; Wang, X.; et al. Two-Dimensional Metal–Organic Framework Superstructures from Ice-Templated Self-Assembly. *J. Am. Chem. Soc.* **2022**, *144*, 17457–17467.
117. Han, W.; Shi, M.; Jiang, H.-L. Scalable and Low-Energy Synthesis of Metal–Organic Frameworks by a Seed-Mediated Approach. *Angew. Chem. Int. Ed.* **2025**, *64*, e202421942.
118. Liu, M.; Lv, Z.; Peng, Y.; et al. Unlocking Advanced Architectures of Single-Crystal Metal–Organic Frameworks. *Angew. Chem. Int. Ed.* **2025**, *64*, e202423939.
119. Łuczak, J.; Kroczewska, M.; Baluk, M.; et al. Morphology Control through the Synthesis of Metal-Organic Frameworks. *Adv. Colloid Interface Sci.* **2023**, *314*, 102864.
120. Su, Y.; Zhang, Y.; Feng, W.; et al. Monocarboxylic Acid Structural Analogues Facilitate *In situ* Composite of Functional Complexes for Aqueous Batteries. *Angew. Chem. Int. Ed.* **2025**, *64*, e202502752.
121. Zhou, T.; Liu, H.; Xia, T.; et al. Optimizing *CO/CO Supply by Atomically Dispersed Fe Sites for High-Rate CO_2-to-C_2H_4 Conversion under Visible Light. *Angew. Chem. Int. Ed.* **2025**, *64*, e202517013.
122. Gao, Y.; Sun, M.; Jing, Y.; et al. Electrocatalytic C–S Cross-Coupling via Engineered Frustrated Lewis Acid-Base Pairs for High-Efficiency Methanesulfonate Synthesis. *Angew. Chem. Int. Ed.* **2025**, *64*, e202509851.
123. Li, L.; Zhao, X.; Tang, M.; et al. Highly Efficient CO_2 Electroreduction in Artificial Seawater Electrolyte Catalyzed by Strong-Acid/Base-Resistant MOF. *Angew. Chem. Int. Ed.* **2025**, *64*, e202512100.
124. Wang, X.; Zhou, W.; Zhai, S.; et al. Metal-Organic Frameworks: Direct Synthesis by Organic Acid-Etching and Reconstruction Disclosure as Oxygen Evolution Electrocatalysts. *Angew. Chem. Int. Ed.* **2024**, *63*, e202400323.
125. Tang, C.; Rao, H.; Li, S.; et al. A Review of Metal–Organic Frameworks Derived Hollow-Structured Photocatalysts: Synthesis and Applications. *Small* **2024**, *20*, 2405533.
126. Kan, X.; Zhang, G.; Ma, J.; et al. Multiscale Co-Assembly to Meso-Macroporous Foamed Single-Crystal Metal–Organic Frameworks for the Supported Capture of Sulfur Dioxide. *Adv. Funct. Mater.* **2024**, *34*, 2312044.
127. Ji, Z.; Mukherjee, S.; Andreo, J.; et al. Electrostatic Atlas of Non-Covalent Interactions Built into Metal–Organic Frameworks. *Nat. Chem.* **2025**, *17*, 1920–1927.

128. Lv, Z.; Lin, R.; Yang, Y.; et al. Uniform Single-Crystal Mesoporous Metal–Organic Frameworks. *Nat. Chem.* **2025**, *17*, 177–185.
129. Jiang, N.; Darù, A.; Kunstelj, Š.; et al. Catalytic, Spectroscopic, and Theoretical Studies of Fe_4S_4-Based Coordination Polymers as Heterogenous Coupled Proton–Electron Transfer Mediators for Electrocatalysis. *J. Am. Chem. Soc.* **2024**, *146*, 12243–12252.
130. Xie, J.; Wang, L.; Anderson, J.S. Heavy Chalcogenide-Transition Metal Clusters as Coordination Polymer Nodes. *Chem. Sci.* **2020**, *11*, 8350–8372.
131. Gillen, J.H.; Moore, C.A.; Vuong, M.; et al. Synthesis and Disassembly of an Organometallic Polymer Comprising Redox-Active Co_4S_4 Clusters and Janus Biscarbene Linkers. *Chem. Commun.* **2022**, *58*, 4885–4888.
132. Kalaj, M.; Cohen, S.M. Postsynthetic Modification: An Enabling Technology for the Advancement of Metal–Organic Frameworks. *ACS Cent. Sci.* **2020**, *6*, 1046–1057.
133. Xie, H.; Khoshooei, M.A.; Mandal, M.; et al. Introducing Metal–Sulfur Active Sites in Metal–Organic Frameworks via Post-Synthetic Modification for Hydrogenation Catalysis. *Nat. Chem.* **2025**, *17*, 1795.
134. Su, Y.; Yuan, G.; Hu, J.; et al. Thiosalicylic-Acid-Mediated Coordination Structure of Nickel Center via Thermodynamic Modulation for Aqueous Ni–Zn Batteries. *Adv. Mater.* **2024**, *36*, 2406094.
135. Smith, K.T.; Yadav, A.K.; Stylianou, K.C. Uncapping Energy Transfer Pathways in Metal-Organic Frameworks through Heterogeneous Structures. *Nat. Commun.* **2025**, *16*, 7986.
136. He, Y.; Tilocca, A.; Dulub, O.; et al. Local Ordering and Electronic Signatures of Submonolayer Water on Anatase TiO_2(101). *Nat. Mater.* **2009**, *8*, 585–589.
137. Castells-Gil, J.; Padial, N.M.; Almora-Barrios, N.; et al. De Novo Synthesis of Mesoporous Photoactive Titanium(iv)–Organic Frameworks with MIL-100 Topology. *Chem. Sci.* **2019**, *10*, 4313–4321.
138. Han, G.; Sun, M.; Zhao, R.; et al. Defect Engineered Ti-MOFs and Their Applications. *Chem. Soc. Rev.* **2025**, *54*, 5081–5107.
139. Serre, C.; Groves, J.A.; Lightfoot, P.; et al. Synthesis, Structure and Properties of Related Microporous N,N'-Piperazinebismethylenephosphonates of Aluminum and Titanium. *Chem. Mater.* **2006**, *18*, 1451–1457.
140. Rozes, L.; Steunou, N.; Fornasieri, G.; et al. Titanium-Oxo Clusters, Versatile Nanobuilding Blocks for the Design of Advanced Hybrid Materials. *Monatshefte Für Chem. Chem. Mon.* **2006**, *137*, 501–528.
141. Wang, S.; Kitao, T.; Guillou, N.; et al. A Phase Transformable Ultrastable Titanium-Carboxylate Framework for Photoconduction. *Nat. Commun.* **2018**, *9*, 1660.
142. Fu, Y.; Sun, D.; Chen, Y.; et al. An Amine-Functionalized Titanium Metal–Organic Framework Photocatalyst with Visible-Light-Induced Activity for CO_2 Reduction. *Angew. Chem. Int. Ed.* **2012**, *51*, 3364–3367.
143. Hendon, C.H.; Tiana, D.; Fontecave, M.; et al. Engineering the Optical Response of the Titanium-MIL-125 Metal–Organic Framework through Ligand Functionalization. *J. Am. Chem. Soc.* **2013**, *135*, 10942–10945.
144. Rozes, L.; Sanchez, C. Titanium Oxo-Clusters: Precursors for a Lego-like Construction of Nanostructured Hybrid Materials. *Chem. Soc. Rev.* **2011**, *40*, 1006–1030.
145. Wang, S.; Cabrero-Antonino, M.; Navalón, S.; et al. A Robust Titanium Isophthalate Metal-Organic Framework for Visible-Light Photocatalytic CO_2 Methanation. *Chem* **2020**, *6*, 3409–3427.
146. Yuan, S.; Liu, T.; Feng, D.; et al. A Single Crystalline Porphyrinic Titanium Metal–Organic Framework. *Chem. Sci.* **2015**, *6*, 3926–3930.
147. Bryant, J.T.; Logan, M.W.; Chen, Z.; et al. Synergistic Steric and Electronic Effects on the Photoredox Catalysis by a Multivariate Library of Titania Metal–Organic Frameworks. *J. Am. Chem. Soc.* **2023**, *145*, 4589–4600.
148. Gao, L.; Zhang, Z.; Li, J.; et al. Thermal Crystal-to-Crystal Transformation Unlocks $Ti_8O_{10}(OOC)_{12}$-Cluster-Based Metal–Organic Frameworks. *J. Am. Chem. Soc.* **2025**, *147*, 26616–26625.
149. Wu, Y.; Jiang, W.; Xu, W.; et al. Hydroxyl Spillover in Fe–Se Dual-Site Catalysts for Mixed Plastics Assay. *J. Am. Chem. Soc.* **2025**, *147*, 1356–1363.
150. Zhang, W.; Yang, B.; Jackson, B.A.; et al. Integrated Low-Temperature PVC and Polyolefin Upgrading. *Science* **2025**, *390*, 88–94.
151. Zhao, J.; Liu, B.; Xiong, L.; et al. Highly Selective Upcycling of Plastic Mixture Waste by Microwave-Assisted Catalysis over Zn/b-ZnO. *Nat. Commun.* **2025**, *16*, 1726.
152. Wang, M.; Gao, Y.; Yuan, S.; et al. Complete Hydrogenolysis of Mixed Plastic Wastes. *Nat. Chem. Eng.* **2024**, *1*, 376–384.
153. Xiong, D.; He, X.; Liu, X.; et al. Manipulating Dual-Metal Catalytic Activities toward Organic Upgrading in Upcycling Plastic Wastes with Inhibited Oxygen Evolution. *ACS Nano* **2024**, *18*, 20340–20352.
154. Ren, S.; Xu, X.; Hu, K.; et al. Salt-Templated Transformation of Waste Plastics into Single-Atom Catalysts for Environmental and Energy Applications. *Nat. Commun.* **2025**, *16*, 8194.
155. Xiong, D.; He, X.; Zhu, Z.; et al. Upcycling Polybutylene Succinate Waste to Succinic Acid via Paired Electrocatalytic Using Thiol-Engineered MOFs and a CO_2-Assisted Precipitation System. *Adv. Funct. Mater.* **2025**, e18434. https://doi.org/10.1002/adfm.202518434.

156. He, D.; Huang, G.; Zhou, Z.; et al. Recent Progress for Designing of Catalysts for Photothermal Conversion of Plastic Wastes. *Adv. Funct. Mater.* **2024**, *36*, 2419801.
157. Ran, H.; Zhang, S.; Ni, W.; et al. Precise Activation of C–C Bonds for Recycling and Upcycling of Plastics. *Chem. Sci.* **2024**, *15*, 795–831.
158. Zhao, J.; Hu, Q.; Wang, Y.; et al. Tandem Catalysis to Mitigate Coke Formation in the Upcycling of Mixed Polyolefin Wastes. *J. Am. Chem. Soc.* **2025**, *147*, 30768–30776.
159. Healy, C.; Patil, K.M.; Wilson, B.H.; et al. The Thermal Stability of Metal-Organic Frameworks. *Coord. Chem. Rev.* **2020**, *419*, 213388.
160. An, Y.; Lv, X.; Jiang, W.; et al. The Stability of MOFs in Aqueous Solutions—Research Progress and Prospects. *Green Chem. Eng.* **2024**, *5*, 187–204.
161. Wu, K.; Liu, X.; Cheng, P.; et al. Linker Engineering for Reactive Oxygen Species Generation Efficiency in Ultra-Stable Nickel-Based Metal–Organic Frameworks. *J. Am. Chem. Soc.* **2023**, *145*, 18931–18938.
162. Yue, K.; Lu, R.; Gao, M.; et al. Polyoxometalated Metal-Organic Framework Superstructure for Stable Water Oxidation. *Science* **2025**, *388*, 430–436.
163. Soni, V.K.; Singh, G.; Vijayan, B.K.; et al. Thermochemical Recycling of Waste Plastics by Pyrolysis: A Review. *Energy Fuels* **2021**, *35*, 12763–12808.
164. Hussain, I.; Aitani, A.; Malaibari, Z.; et al. Chemical Upcycling of Waste Plastics to High Value-Added Products via Pyrolysis: Current Trends, Future Perspectives, and Techno-Feasibility Analysis. *Chem. Rec.* **2023**, *23*, e202200294.
165. Li, H.; Wu, J.; Jiang, Z.; et al. Hydroformylation of Pyrolysis Oils to Aldehydes and Alcohols from Polyolefin Waste. *Science* **2023**, *381*, 660–666.
166. Cannavacciuolo, F.D.; Yadav, R.; Esper, A.; et al. A High-Throughput Approach to Repurposing Olefin Polymerization Catalysts for Polymer Upcycling. *Angew. Chem. Int. Ed.* **2022**, *61*, e202202258.
167. Chen, S.; Tennakoon, A.; You, K.-E.; et al. Ultrasmall Amorphous Zirconia Nanoparticles Catalyse Polyolefin Hydrogenolysis. *Nat. Catal.* **2023**, *6*, 161–173.
168. Klet, R.C.; Tussupbayev, S.; Borycz, J.; et al. Single-Site Organozirconium Catalyst Embedded in a Metal–Organic Framework. *J. Am. Chem. Soc.* **2015**, *137*, 15680–15683.
169. Ji, P.; Solomon, J.B.; Lin, Z.; et al. Transformation of Metal–Organic Framework Secondary Building Units into Hexanuclear Zr-Alkyl Catalysts for Ethylene Polymerization. *J. Am. Chem. Soc.* **2017**, *139*, 11325–11328.
170. Uemura, T.; Yanai, N.; Kitagawa, S. Polymerization Reactions in Porous Coordination Polymers. *Chem. Soc. Rev.* **2009**, *38*, 1228–1236.
171. Heng, J.Z.X.; Tan, T.T.Y.; Li, X.; et al. Pyrolytic Depolymerization of Polyolefins Catalysed by Zirconium-Based UiO-66 Metal–Organic Frameworks. *Angew. Chem. Int. Ed.* **2024**, *63*, e202408718.
172. Artetxe, M.; Lopez, G.; Amutio, M.; et al. Cracking of High Density Polyethylene Pyrolysis Waxes on HZSM-5 Catalysts of Different Acidity. *Ind. Eng. Chem. Res.* **2013**, *52*, 10637–10645.
173. Wang, Y.; Cheng, L.; Gu, J.; et al. Catalytic Pyrolysis of Polyethylene for the Selective Production of Monocyclic Aromatics over the Zinc-Loaded ZSM-5 Catalyst. *ACS Omega* **2022**, *7*, 2752–2765.
174. Hou, Q.; Zhen, M.; Qian, H.; et al. Upcycling and Catalytic Degradation of Plastic Wastes. *Cell Rep. Phys. Sci.* **2021**, *2*, 100514.
175. Guo, Z.; Zhang, H.; Chen, H.; et al. Hydrogenating Polyethylene Terephthalate into Degradable Polyesters. *Angew. Chem. Int. Ed.* **2025**, *64*, e202418157.
176. Wen, X.; Niu, R.; Tang, T.; et al. Atmospheric, Continuous Degradation of Poly(ethylene terephthalate) Waste by ZnO. *Appl. Catal. B Environ.* **2025**, *377*, 125485.
177. Thiounn, T.; Smith, R.C. Advances and Approaches for Chemical Recycling of Plastic Waste. *J. Polym. Sci.* **2020**, *58*, 1347–1364.
178. Cao, J.; Liang, H.; Yang, J.; et al. Depolymerization Mechanisms and Closed-Loop Assessment in Polyester Waste Recycling. *Nat. Commun.* **2024**, *15*, 6266.
179. Qin, M.; Huang, P.; Zhang, M.; et al. Binuclear Metal-Based Covalent Organic Framework Mimicking Metallohydrolases for Direct Photoreforming of PET Plastic. *J. Am. Chem. Soc.* **2025**, *147*, 29232–29240.
180. Wu, B.; Zhong, B.; Zheng, L.; et al. Harnessing Protein Language Model for Structure-Based Discovery of Highly Efficient and Robust PET Hydrolases. *Nat. Commun.* **2025**, *16*, 6211.
181. Robles-Martín, A.; Amigot-Sánchez, R.; Fernandez-Lopez, L.; et al. Sub-Micro- and Nano-Sized Polyethylene Terephthalate Deconstruction with Engineered Protein Nanopores. *Nat. Catal.* **2023**, *6*, 1174–1185.
182. Zhang, S.; Xu, W.; Zhao, X.; et al. Adjustable Upcycling of Polyethylene Terephthalate to Biodegradable Polymer Monomers by Mn-Catalyzed Solvent Switching Strategy. *Angew. Chem. Int. Ed.* **2025**, *64*, e202505490.
183. Chen, X.; Guo, Z.; Wang, L.; et al. Directional-Path Modification Strategy Enhances PET Hydrolase Catalysis of Plastic Degradation. *J. Hazard. Mater.* **2022**, *433*, 128816.

184. Cao, Y.; Xiang, L.; Nikodinovic-Runic, J.; et al. Improving Enzymatic Degradation of Unpretreated Poly(ethylene terephthalate). *Chin. J. Catal.* **2025**, *71*, 375–389.
185. Jin, S.; Kwon, C.; Bugaev, A.; et al. Atom-by-Atom Design of Cu/ZrO_x Clusters on MgO for CO_2 Hydrogenation Using Liquid-Phase Atomic Layer Deposition. *Nat. Catal.* **2024**, *7*, 1199–1212.
186. Chen, S.; Zhu, Z.; Song, K.; et al. Engineering Cu/Ru Heterointerface-Shelled Nanocavities by the Kirkendall Effect for Highly Efficient Nitrate Electroreduction to Ammonia. *J. Am. Chem. Soc.* **2025**, *147*, 36494–36507.
187. Trickett, C.A.; Osborn Popp, T.M.; Su, J.; et al. Identification of the Strong Brønsted Acid Site in a Metal–Organic Framework Solid Acid Catalyst. *Nat. Chem.* **2019**, *11*, 170–176.
188. Kirlikovali, K.O.; Chen, Z.; Islamoglu, T.; et al. Zirconium-Based Metal–Organic Frameworks for the Catalytic Hydrolysis of Organophosphorus Nerve Agents. *ACS Appl. Mater. Interfaces* **2020**, *12*, 14702–14720.
189. Li, J.; Huang, J.; Zhao, Z.; et al. Low-Coordination Indium Single-Atom Sites Anchored on a Metal-Organic Framework Single-Layer Boosts Electroreduction of CO_2 into Formic Acid. *Angew. Chem. Int. Ed.* **2025**, *64*, e202511132.
190. Chi, H.; Song, S.; Zhao, K.; et al. Non-Van-der-Waals Oriented Two-Dimensional UiO-66 Films by Rapid Aqueous Synthesis at Room Temperature. *J. Am. Chem. Soc.* **2025**, *147*, 7255–7263.
191. Bai, Y.; Dou, Y.; Xie, L.; et al. Zr-Based Metal–Organic Frameworks: Design, Synthesis, Structure, and Applications. *Chem. Soc. Rev.* **2016**, *45*, 2327–2367.
192. Xiong, X.; Song, L.; Wang, W.; et al. Synthesis and Modification of Formate Zr-MOF (ZrFA) toward Scalable and Cost-Cutting Gas Separation. *Angew. Chem. Int. Ed.* **2025**, *64*, e202505978.
193. Wu, Y.; Wang, X.; Kirlikovali, K.O.; et al. Catalytic Degradation of Polyethylene Terephthalate Using a Phase-Transitional Zirconium-Based Metal–Organic Framework. *Angew. Chem. Int. Ed.* **2022**, *61*, e202117528.
194. Guillerm, V.; Ragon, F.; Dan-Hardi, M.; et al. A Series of Isoreticular, Highly Stable, Porous Zirconium Oxide Based Metal–Organic Frameworks. *Angew. Chem. Int. Ed.* **2012**, *51*, 9267–9271.
195. Kratish, Y.; Li, J.; Liu, S.; et al. Polyethylene Terephthalate Deconstruction Catalyzed by a Carbon-Supported Single-Site Molybdenum-Dioxo Complex. *Angew. Chem. Int. Ed.* **2020**, *59*, 19857–19861.
196. Xu, M.; Chen, Q.; Xie, L.; et al. Exchange Reactions in Metal-Organic Frameworks: New Advances. *Coord. Chem. Rev.* **2020**, *421*, 213421.
197. Wei, X.; Qiu, J.; Wang, H.; et al. Efficient Glycolysis of Poly(ethylene terephthalate) to Bis(hydroxyethyl) Terephthalate Catalyzed by Non-Metallic Deep Eutectic Solvent. *Chem. Eng. J.* **2025**, *508*, 161115.
198. Wu, Y.; Tang, X.; Qian, S.; et al. Efficient Chemical Recycling of Mixed Plastics by Intramolecular Glycolysis. *AIChE J.* **2025**, *71*, e70064.
199. Barnard, E.; Rubio Arias, J.J.; Thielemans, W. Chemolytic Depolymerisation of PET: A Review. *Green Chem.* **2021**, *23*, 3765–3789.
200. Jo, Y.; Kim, E.J.; Kim, J.; et al. Efficient Fe_3O_4 Nanoparticle Catalysts for Depolymerization of Polyethylene Terephthalate. *Green Chem.* **2023**, *25*, 8160–8171.
201. Chiao, Y.-W.; Liao, W.; Krisbiantoro, P.A.; et al. Waste-Battery-Derived Multifunctional Zinc Catalysts for Glycolysis and Decolorization of Polyethylene Terephthalate. *Appl. Catal. B* **2023**, *325*, 122302.
202. Suo, Q.; Zi, J.; Bai, Z.; et al. The Glycolysis of Poly(ethylene terephthalate) Promoted by Metal Organic Framework (MOF) Catalysts. *Catal. Lett.* **2017**, *147*, 240–252.
203. Ghaemy, M.; Mossaddegh, K. Depolymerisation of Poly(ethylene terephthalate) Fibre Wastes Using Ethylene Glycol. *Polym. Degrad. Stab.* **2005**, *90*, 570–576.
204. Han, N.; Lee, K.; Lee, J.; et al. Dual-Porous ZIF-8 Heterogeneous Catalysts with Increased Reaction Sites for Efficient PET Glycolysis. *Chemosphere* **2024**, *364*, 143187.
205. Yang, R.; Bieh, Y.; Chen, C.H.; et al. Heterogeneous Metal Azolate Framework-6 (MAF-6) Catalysts with High Zinc Density for Enhanced Polyethylene Terephthalate (PET) Conversion. *ACS Sustain. Chem. Eng.* **2021**, *9*, 6541–6550.
206. Park, K.S.; Ni, Z.; Côté, A.P.; et al. Exceptional Chemical and Thermal Stability of Zeolitic Imidazolate Frameworks. *Proc. Natl. Acad. Sci. USA* **2006**, *103*, 10186–10191.
207. Apicella, B.; Di Serio, M.; Fiocca, L.; et al. Kinetic and Catalytic Aspects of the Formation of Poly(ethylene terephthalate) (PET) Investigated with Model Molecules. *J. Appl. Polym. Sci.* **1998**, *69*, 2423–2433.
208. Reinoso, D.M.; Ferreira, M.L.; Tonetto, G.M. Study of the Reaction Mechanism of the Transesterification of Triglycerides Catalyzed by Zinc Carboxylates. *J. Mol. Catal. A Chem.* **2013**, *377*, 29–41.
209. Liu, B.; Fu, W.; Lu, X.; et al. Lewis Acid–Base Synergistic Catalysis for Polyethylene Terephthalate Degradation by 1,3-Dimethylurea/$Zn(OAc)_2$ Deep Eutectic Solvent. *ACS Sustain. Chem. Eng.* **2019**, *7*, 3292–3300.
210. Cao, J.; Chen, W.; Jiang, W.; et al. Sustainable Closed-Loop Recycling of Polyester Waste Using Reconstructed Defective-Metal–Organic Frameworks. *Angew. Chem. Int. Ed.* **2025**, *64*, e202504743.
211. Wang, A.; Zhang, L.; Rahimi, M.G.; et al. Defect Engineering of ZnO for Electron Transfer in O_3 Catalytic Decomposition. *Appl. Catal. B* **2020**, *277*, 119223.

212. An, Z.; Zhang, Z.; Huang, Z.; et al. Pt_1 Enhanced C–H Activation Synergistic with Pt_n Catalysis for Glycerol Cascade Oxidation to Glyceric Acid. *Nat. Commun.* **2022**, *13*, 5467.
213. Liu, K.; Gao, X.; Liu, C.-X.; et al. Energy-Saving Hydrogen Production by Seawater Splitting Coupled with PET Plastic Upcycling. *Adv. Energy Mater.* **2024**, *14*, 2304065.
214. Yang, S.; Li, Y.; Nie, M.; et al. Lifecycle Management for Sustainable Plastics: Recent Progress from Synthesis, Processing to Upcycling. *Adv. Mater.* **2024**, *36*, 2404115.
215. Chu, S.; Zhang, B.; Zhao, X.; et al. Photocatalytic Conversion of Plastic Waste: From Photodegradation to Photosynthesis. *Adv. Energy Mater.* **2022**, *12*, 2200435.
216. Jiao, X.; Zheng, K.; Chen, Q.; et al. Photocatalytic Conversion of Waste Plastics into C_2 Fuels under Simulated Natural Environment Conditions. *Angew. Chem. Int. Ed.* **2020**, *59*, 15497–15501.
217. Deng, X.; Zhang, J.; Qi, K.; et al. Ultrafast Electron Transfer at the In_2O_3/Nb_2O_5 S-Scheme Interface for CO_2 Photoreduction. *Nat. Commun.* **2024**, *15*, 4807.
218. Jiang, M.; Li, J.; Wan, X.; et al. Floatable Organic-Inorganic Hybrid-TiO_2 Unlocks Superoxide Radicals for Plastic Photoreforming in Neutral Solution. *Nat. Commun.* **2025**, *16*, 4136.
219. Zhou, X.; Cao, K.; Huang, S.; et al. Synergistic Conversion of Hydrogen Peroxide and Benzaldehyde in Air by Silver Single-Atom Modified Thiophene-Functionalized g-C_3N_4. *Angew. Chem. Int. Ed.* **2025**, *64*, e202505532.
220. Su, Y.; Yuan, G.; Hu, J.; et al. Recent Progress in Strategies for Preparation of Metal-Organic Frameworks and Their Hybrids with Different Dimensions. *Chem. Synth.* **2023**, *3*, 1.
221. Munyaneza, N.E.; Ji, R.; DiMarco, A.; et al. Chain-Length-Controllable Upcycling of Polyolefins to Sulfate Detergents. *Nat. Sustain.* **2024**, *7*, 1681–1690.
222. Sun, B.; Zou, J.; Qiu, W.; et al. Chemical Transformation of Polyurethane into Valuable Polymers. *Natl. Sci. Rev.* **2024**, *12*, nwae393.
223. Kang, Y.; Lee, W.; Bae, T.; et al. Harnessing Large Language Models to Collect and Analyze Metal–Organic Framework Property Data Set. *J. Am. Chem. Soc.* **2025**, *147*, 3943–3958.
224. Wang, C.; Zhang, Z.; Yi, X. MOFs-Based Functional Materials for Aqueous Micro/Nanoplastics Elimination. *Chin. Chem. Lett.* **2023**, *34*, 108182.
225. Zhang, W.; Han, Y.; Yang, F.; et al. A Customized Self-Assembled Synergistic Biocatalyst for Plastic Depolymerization. *J. Hazard. Mater.* **2024**, *477*, 135380.
226. Chen, K.; Lu, G.; Duan, X.; et al. MOFs-Derived Porous Co-NC for Rapid and High-Capacity Removal of Nanoplastics. *Sep. Purif. Technol.* **2025**, *363*, 132008.
227. Qin, J.; Zhou, J.; Ma, J.; et al. Breaking Symmetry of Active Sites in Metal-Organic Frameworks for Efficient Photocatalytic Valorization of Polyester Plastics. *Angew. Chem. Int. Ed.* **2025**, *64*, e202505786.
228. Qin, J.; Dou, Y.; Zhou, J.; et al. Photocatalytic Valorization of Plastic Waste over Zinc Oxide Encapsulated in a Metal–Organic Framework. *Adv. Funct. Mater.* **2023**, *33*, 2214839.
229. Zhou, A.; Dou, Y.; Zhao, C.; et al. A Leaf-Branch TiO_2/Carbon@MOF Composite for Selective CO_2 Photoreduction. *Appl. Catal. B* **2020**, *264*, 118519.
230. Thompson, R.C.; Olsen, Y.; Mitchell, R.P.; et al. Lost at Sea: Where is All the Plastic? *Science* **2004**, *304*, 838.
231. Lin, J.; Hu, K.; Wang, Y.; et al. Tandem Microplastic Degradation and Hydrogen Production by Hierarchical Carbon Nitride-Supported Single-Atom Iron Catalysts. *Nat. Commun.* **2024**, *15*, 8769.
232. Sun, Y.; Peng, M.; Zhang, Q.; et al. Aging of Microplastics and Its Photo-Catalytic Degradation of Coexisting Tetracycline. *Sep. Purif. Technol.* **2025**, *355*, 129605.
233. Yang, C.; Duan, J.; Song, J.; et al. New Insights for Microplastic Degradation: Synergistic Degradation Mechanisms of Microplastics and Atrazine in Sediments. *Water Res.* **2025**, *287*, 124396.
234. Zhang, S.; Li, P.; Hu, Q.; et al. Diatomic Zn-Functionalized Carbon Sphere for Microplastics Remediation in Natural Seawater at Environmentally Relevant Concentration. *Adv. Mater.* **2025**, *37*, e08428.
235. Feng, Y.; Yu, Y.; Xi, T.; et al. Scalable Bamboo Fiber/Microfibrillated Cellulose Foam via Solvent-Exchange-Assisted Ambient Drying for Highly Efficient Microplastics Capture. *Adv. Funct. Mater.* **2025**, e14273. https://doi.org/10.1002/adfm.202514273.
236. Wu, Y.; Chen, S.; Wu, J.; et al. Revivable Self-Assembled Supramolecular Biomass Fibrous Framework for Efficient Microplastic Removal. *Sci. Adv.* **2024**, *10*, eadn8662.
237. Chen, Z.; Wei, W.; Ni, B.-J. Prioritizing Capture and Utilization for Microplastic Management in Water Systems. *Nat. Rev. Clean Technol.* **2025**, *1*, 525–527.
238. Kim, J.; Jang, J.; Hilberath, T.; et al. Photoelectrocatalytic Biosynthesis Fuelled by Microplastics. *Nat. Synth.* **2022**, *1*, 776–786.
239. Zandieh, M.; Liu, J. Removal and Degradation of Microplastics Using the Magnetic and Nanozyme Activities of Bare Iron Oxide Nanoaggregates. *Angew. Chem. Int. Ed.* **2022**, *61*, e202212013.

240. Ni, R.; Zhang, L.; Ma, J.; et al. Versatile Keratin Fibrous Adsorbents with Rapid-Response Shape-Memory Features for Sustainable Water Remediation. *Nano Lett.* **2024**, *24*, 12891–12899.
241. Song, Y.; Zhu, W.; Wang, C.; et al. Nanoarchitectonics of Metal–Organic Framework and Nanocellulose Composites for Multifunctional Environmental Remediation. *Adv. Mater.* **2025**, *37*, 2504364.
242. Bayo, J.; López-Castellanos, J.; Doval-Miñarro, M.; et al. Eco-Labeled Composts Reduce Microplastic Contamination and Mitigate Heavy Metal Bioavailability in Agricultural Ecosystems. *Sci. Rep.* **2025**, *15*, 32793.
243. Yang, A.; Pei, H.; Zhang, M.; et al. Molecular Mechanisms by Which Polyethylene Terephthalate (PET) Microplastic and PET Leachate Promote the Growth of Benthic Cyanobacteria. *Water Res.* **2025**, *280*, 123476.
244. Jiang, X.; Gu, G.; Liu, Y.; et al. Binary Transport of PS and PET Microplastics in Saturated Quartz Sand: Effect of Sand Particle Size and PET Shape. *J. Hazard. Mater.* **2025**, *496*, 139265.
245. Li, Y.; Zhang, J.; Xu, L.; et al. Leaf Absorption Contributes to Accumulation of Microplastics in Plants. *Nature* **2025**, *641*, 666–673.
246. Yu, T.; Huang, X.; Zhang, X.F.; et al. A Review of Nanomaterials with Excellent Purification Potential for the Removal of Micro- and Nanoplastics from Liquid. *DeCarbon* **2024**, *5*, 100064.
247. Zhou, G.; Xu, H.; Song, H.; et al. Photocatalysis toward Microplastics Conversion: A Critical Review. *ACS Catal.* **2024**, *14*, 8694–8719.
248. Ho, K.L.; Yeap, S.P.; Lee, K.M. A Critical Review of Microplastics and Nanoplastics in Wastewater: Insights into Adsorbent-Based Remediation Strategies. *Environ. Pollut.* **2025**, *382*, 126658.
249. Huang, K.; Xie, L.; Gu, X.; et al. Comprehensive Assessment of Various Digestion Protocols for Extraction Microplastics from Organic-Rich Environmental Matrices. *Water Res.* **2025**, *282*, 123935.
250. Huang, Y.; Wang, Q.; Xin, Q.; et al. Enhancement Mechanism of Chitosan/Tannic Acid Curing and Functional Group Modification on Uranium Adsorption in Five Types of Wastewater by Cu-MOF. *J. Hazard. Mater.* **2025**, *492*, 138185.
251. Wan, H.; Wang, J.; Sheng, X.; et al. Removal of Polystyrene Microplastics from Aqueous Solution Using the Metal–Organic Framework Material of ZIF-67. *Toxics* **2022**, *10*, 70.
252. Cong, S.; Sun, S.; Zhang, Y.; et al. Regulating the Growth Orientation of ZIF-L Membrane for H_2/CO_2 Separation. *Adv. Funct. Mater.* **2025**, *36*, e15548.
253. Lin, Z.; Liu, G.; Sheng, B.; et al. Capture and Removal of Nanoplastics Using ZIF-Derived Defective Nanoframework: Structure-Performance Correlation, Theoretical Calculation and Application. *Nano Today* **2024**, *58*, 102418.
254. Chen, Y.-J.; Chen, Y.; Miao, C.; et al. Metal–Organic Framework-Based Foams for Efficient Microplastics Removal. *J. Mater. Chem. A* **2020**, *8*, 14644–14652.
255. Pasanen, F.; Fuller, R.O.; Maya, F. Fast and Simultaneous Removal of Microplastics and Plastic-Derived Endocrine Disruptors Using a Magnetic ZIF-8 Nanocomposite. *Chem. Eng. J.* **2023**, *455*, 140405.
256. Feng, J.; Dong, Y.; Li, H.; et al. Engineered Magnetic Metal-Organic Frameworks for Efficient and Broad-Spectrum Adsorption of Micro/Nanoplastics in Beverages. *J. Hazard. Mater.* **2025**, *495*, 139040.
257. Jiang, H.; Moosavi, S.M.; Czaban-Jóźwiak, J.; et al. Reticular Chemistry for the Rational Design of Mechanically Robust Mesoporous Merged-Net Metal-Organic Frameworks. *Matter* **2023**, *6*, 285–295.
258. Chen, H.; Zhao, Z.; Huang, N.; et al. Rational Design and Synthesis of a Metal–Organic Framework Featuring Cu(I)–Carbon Bonds for Enhanced Artificial Photosynthesis. *J. Am. Chem. Soc.* **2025**, *147*, 38484–38491.
259. Wang, K.; Zhang, Y.; Gong, Z.; et al. Monolayered Metal–Organic Framework Unlocks Integration of Shaped Nanoparticles for Synergistic Photocatalysis. *J. Am. Chem. Soc.* **2025**, *147*, 24241–24247.
260. Liu, S.; Tian, L.; Han, L.; et al. Bimetallic Co/Fe-MOF Derived from Poly(butylene adipate-co-terephthalate) (PBAT) Plastic Wastes for Efficient Interfacial Solar Steam Generation. *Desalination* **2025**, *614*, 119118.
261. Qu, W.; Jin, T.; Huang, K.; et al. Metal–Organic Frameworks-Driven Atomic Precision in Advanced Oxidation for Pollution Control. *Adv. Mater.* **2025**, *38,* e12877.
262. Song, X.; Jallow, J.; Basheer, C.; et al. Microdroplet-Driven Synthesis of a Metal–Organic Framework Catalyst. *Angew. Chem. Int. Ed.* **2025**, *64*, e202515006.
263. Ni, Y.; Xie, W.; Yan, Z.; et al. Spatially-Directed C–C Coupling Inside Three-Dimensional Metal-Organic Frameworks for CO_2 Electroreduction to C_2 Products. *Angew. Chem. Int. Ed.* **2025**, *64*, e202518398.
264. Bai, W.; Shao, Q.; Ji, Y.; et al. Pd–N_4 Sites in MOFs Modulate Oxygen Reduction Pathways for 100% Selective Photocatalytic CO_2-to-CH_4 Conversion from Oxygenated Flue Gas. *Angew. Chem. Int. Ed.* **2025**, *137*, e202513157.
265. Li, Z.; Wang, Y.; Wei, X.; et al. Kg-Scale Synthesis of Ultrathin Single-Crystalline MOF/GO/MOF Sandwich Nanosheets with Elevated Electrochemical Performance. *Adv. Mater.* **2025**, *37*, 2505700.